The Astrophysical Journal, 780:165 (15pp), 2014 January 10 doi:10.1088/0004-637X/780/2/165

JET EMISSION IN YOUNG RADIO SOURCES: A *FERMI* LARGE AREA TELESCOPE GAMMA-RAY VIEW

G. Migliori[1], A. Siemiginowska[1], B. C. Kelly[2], Ł. Stawarz[3,4], A. Celotti[5,6,7], and M. C. Begelman[8]
[1] Harvard-Smithsonian Center for Astrophysics, 60 Garden St., Cambridge, MA 02138, USA; migliori@cfa.harvard.edu
[2] Department of Physics, Broida Hall, University of California, Santa Barbara, CA 93107, USA
[3] Institute of Space and Astronautical Science, JAXA, 3-1-1 Yoshinodai, Chuo-ku, Sagamihara, Kanagawa 252-5210, Japan
[4] Astronomical Observatory, Jagiellonian University, 30-244 Kraków, Poland
[5] Scuola Internazionale Superiore di Studi Avanzati (SISSA), via Bonomea, 265-34136 Trieste, Italy
[6] INAF-Osservatorio Astronomico di Brera, via E. Bianchi 46, I-23807 Merate, Italy
[7] INFN- Sezione di Trieste, via Valerio 2, I-34127, Trieste, Italy
[8] JILA, University of Colorado and National Institute of Standards and Technology, 440 UCB, Boulder, CO 80309-0440, USA
Received 2013 July 10; accepted 2013 November 21; published 2013 December 20

ABSTRACT

We investigate the contribution of the beamed jet component to the high-energy emission in young and compact extragalactic radio sources, focusing for the first time on the γ-ray band. We derive predictions on the γ-ray luminosities associated with the relativistic jet assuming a leptonic radiative model. The high-energy emission is produced via Compton scattering by the relativistic electrons in a spherical region at the considered scales ($\lesssim$10 kpc). Simulations show a wide range of γ-ray luminosities, with intensities up to $\sim 10^{46}$–10^{48} erg s^{-1} depending on the assumed jet parameters. We find a highly linear relation between the simulated X-ray and γ-ray luminosities that can be used to select candidates for γ-ray detection. We compare the simulated luminosity distributions in the radio, X-ray, and γ-ray regimes with observations for the largest sample of X-ray-detected young radio quasars. Our analysis of $\sim$4-yr *Fermi* Large Area Telescope (LAT) data does not yield any statistically significant detections. However, the majority of the model-predicted γ-ray fluxes for the sample are near or below the current *Fermi*-LAT flux threshold and compatible with the derived upper limits. Our study gives constraints on the minimum jet power ($L_{\rm jet,kin}/L_{\rm disk} > 0.01$) of a potential jet contribution to the X-ray emission in the most compact sources ($\lesssim$1 kpc) and on the particle-to-magnetic field energy density ratio that are in broad agreement with equipartition assumptions.

Key words: galaxies: active – galaxies: jets – gamma rays: galaxies – radiation mechanisms: non-thermal

Online-only material: color figures

1. INTRODUCTION

Young and compact radio sources represent the first stage in the evolution of large extragalactic radio sources and constitute an important fraction ($\sim$10%–30%) of the radio source population (see, however, Stanghellini et al. 2005; Tinti et al. 2005 for problems in selecting genuine young sources against blazars). There are still open questions on the radio source initial phase concerning its impact on the host galaxy and the evolutionary path from compact to large (and giant) radio structures.

Simulations indicate that during the first phase of the expansion, which lasts $\approx 10^5$ yr, a powerful radio source can interact with the interstellar medium (ISM) of its host galaxy and later on with the intergalactic medium (IGM; Bicknell & Sutherland 2006; Wagner et al. 2012 and references therein). Observations at radio and optical frequencies reveal signatures of these interactions in nearby radio galaxies (e.g., Tadhunter 2007; Holt et al. 2008; Labiano 2008; Holt et al. 2011; Siemiginowska et al. 2012; Liuzzo et al. 2013). Both the mechanical and radiative energies released by the young radio source can be relatively high and may have an important impact on the host galaxy (e.g., influencing the star formation processes, affecting the amount and temperature of the gaseous fraction of the ISM and IGM). Measurements of the radio source total power during the initial phase are thus important for unveiling feedback processes at work in the evolving galaxies.

According to the current understanding, compact GigaHertz-Peaked Spectrum (GPS) radio sources evolve into Compact Steep Spectrum (CSS) sources[9] and finally become large-scale ($\gtrsim$20 kpc) radio sources (Fanti et al. 1995; Begelman 1996; Snellen et al. 2000). The presence of a class of even more compact and young radio sources, the so-called High-Frequency Peakers, is still under investigation (Dallacasa et al. 2000; Orienti 2009, for a review). The high fraction of young sources in radio samples (in comparison with the large-scale ones) suggests a more complex evolutionary picture: intermittency of the radio activity (Reynolds & Begelman 1997) or the presence of a population of short-lived sources (never reaching the large-scale stage, e.g., Alexander 2000; Kunert-Bajraszewska et al. 2010, 2013; Orienti et al. 2010) are possible explanations. Furthermore, it is not clear which morphology GPS and CSS sources will finally display, i.e., whether they will evolve into Fanaroff–Riley type I (FRI) or type II (FRII) sources (Fanaroff & Riley 1974).

The high-energy domain may provide important clues on the most energetic processes associated with the young source phase. So far, most of the high-energy investigations have been done in the X-rays (0.5–10 keV) using *Chandra* and *XMM-Newton* observations (Siemiginowska et al. 2008; Tengstrand et al. 2009). These show that young sources are relatively X-ray luminous ($L_X \sim 10^{42}$–10^{46} erg s^{-1}). However, the entire radio structure is typically enclosed within angular scales that cannot be resolved by X-ray telescopes (a few

[9] GPS and CSS radio sources are characterized by a linear size $\lesssim$1 and $\lesssim$10–15 kpc, respectively, and a power at 1.4 GHz $P_{1.4\,\rm GHz} \geqslant 10^{32}$ erg s^{-1} Hz^{-1}. They typically display convex radio spectra with turn-over frequencies between $\sim$0.1 and $\sim$1 GHz (see O'Dea 1998 for a review).

arcseconds or smaller), thus the X-ray morphology is usually not accessible (Siemiginowska 2009). Studies of the origin of the X-ray emission, including an identification of distinct high-energy emission components, rely mainly on the analysis of X-ray spectral features, which is hampered by the limited photon statistics (Guainazzi et al. 2006; Vink et al. 2006; Siemiginowska et al. 2008; Tengstrand et al. 2009). As a consequence, it is hard to disentangle the contribution of the jet- and lobe-related non-thermal emission from the contribution related to the accretion processes (either the X-ray thermal emission of the innermost part of the disk or that resulting from the Comptonization of disk photons by electrons in a hot corona).

A significant level of non-thermal X-ray flux can be produced via inverse Compton (IC) scattering of different seed photons in the compact lobes of GPS radio galaxies (Stawarz et al. 2008). Given the typical GPS linear sizes ($\lesssim$1 kpc) the nuclear photon fields, e.g., optical–ultraviolet disk and infrared (IR) torus photons, are intense enough to provide, when Comptonized, X-ray luminosities of the order of 10^{44}–10^{46} erg s^{-1} (Stawarz et al. 2008; Ostorero et al. 2010). In the case of GPS and CSS quasars, the closer jet alignment to the line of sight should favor the beamed jet component. This is certainly observed in the radio band (Fanti et al. 1990), while the X-ray behavior remains more elusive. The jet X-ray emission can be important depending on its parameters (inclination, bulk motion, intrinsic power). In the case of the CSS quasar 3C 186, we have shown that the jet could contribute to the total X-ray emission when it develops a complex velocity structure (see Migliori et al. 2012).

The γ-ray band can be useful to study many aspects of the physics of young radio sources. At these frequencies, the disk-corona component is expected to rapidly drop in intensity, while both beamed and unbeamed non-thermal emission could be still strong and detectable in powerful sources. The intensity of the γ-ray flux depends on several factors. For the case of compact symmetric objects (CSOs), the model presented in Stawarz et al. (2008) predicts a significant isotropic non-thermal emission in the 0.1–100 GeV band produced in the radio lobes, however, within a wide range from $\sim10^{41}$ erg s^{-1} up to $\sim10^{46}$ erg s^{-1} depending on the source parameters. In this scenario, the non-thermal, high-energy emission may even dominate the total radiative output of the source and as such it is crucial for constraining the total energetics of the expanding source. Ito et al. (2011) and Kino et al. (2013) have shown that non-thermal IC emission may arise from a shell of shocked ISM driven by the expanding radio source. The estimated GeV and TeV emission from the mini shells associated with powerful (i.e., jet powers of the order of $\sim10^{46}$ erg s^{-1}) and compact ($\sim$5 pc) sources could be potentially detectable by the next generation of Cherenkov telescopes. The γ-ray emission related to the hadronic component within the compact lobes of CSOs was discussed in Kino & Asano (2011). Kino et al. (2009) predict bright GeV luminosities produced via bremsstrahlung in the cocoons and radio lobes of CSOs. In this case, a γ-ray detection with *Fermi*-LAT would be possible for nearby ($\lesssim10^2$ Mpc) sources if the jet is powerful and made of $e^{\pm}$ plasma.

A dedicated study of the jet component in young radio sources and its possible γ-ray emission has not yet been performed. We have therefore investigated for the first time the γ-ray properties of a sample of young radio sources using the LAT onboard the *Fermi* satellite (see Atwood et al. 2009). The goals of the study are (1) to refine model predictions for the γ-ray emission of the jets of young radio sources and (2) to constrain the entire non-thermal, high-energy emission continua of these objects. We adopt the following approach: we first set up a general leptonic synchrotron and IC model for the non-thermal emission of jets in compact radio sources and then we generate a library of their broadband spectral energy distributions (SEDs) for a wide range of selected jet parameters (linear sizes, jet powers, jet bulk velocities, etc.). While previous studies focused on the isotropic emission associated with the extended structures of young sources, i.e., lobes and cocoons, in this work we concentrate on the jet-beamed radiation and consider powerful radio quasars. Indeed, an important difference between jet and lobe emission arises from the jet relativistic (bulk) motion: the jet emission is relativistically beamed and its detection also depends on the observers viewing angle. In models presented in the literature (see, e.g., Stawarz et al. 2008; Kino et al. 2009; Ito et al. 2011; Kino & Asano 2011; Kino et al. 2013), the emission of the source is consistently calculated by coupling the evolution of the electron distribution to the source dynamical expansion. Here, rather than following the evolution of a single source, we simulate the emission for a distribution of sources assuming a wide range of values for the jet parameters. These simulations are compared with the analyzed *Fermi*-LAT data for the considered sample of GPS and CSS sources. We discuss the results of the LAT analysis on the sample and the implications for non-thermal models.

2. JET MODEL

We set up a model to evaluate the non-thermal (beamed) emission from jets in young radio sources. The jet emission is computed using a general leptonic radiative model. In the following, we describe the main features of the model.

We assume a simple geometry for the emission region (see Figure 1 for a schematic illustration). The bulk of the jet emission is produced in a spherical knot, located at a distance z_d from the central black hole (BH). The knot is moving with a bulk Lorentz factor Γ. The electrons in the knot radiate via synchrotron and IC emission. Seed photons for the IC mechanism are the synchrotron emission of the knot and external radiation fields (synchrotron self-Compton (SSC) and external Compton (EC) processes, respectively). The latter are ultraviolet (UV) photons from the accretion disk (EC/disk; Dermer et al. 1992) or disk emission reprocessed by the dust surrounding the central engine and emitted at IR wavelengths (EC/dust Błażejowski et al. 2000; Sikora et al. 2009). The model also takes into account the high-energy emission that may be associated with the presence of a longitudinal velocity structure inside the jet. This is done by adding a radiative field of synchrotron photons (EC/syn) produced outside the knot in a blazar-like component located at the base of the jet, moving with a highly relativistic speed $\Gamma_{\rm bl}$ (see Celotti et al. 2001; Migliori et al. 2012). The intensity of EC/syn luminosity can be comparable to the high-energy emission potentially produced by the blazar core itself (e.g., via SSC or Compton scattering of the photons of the broad-line regions, BLRs, and of the dusty torus). Therefore, we included the EC/syn contribution to the total jet high-energy emission only if it is larger than the blazar one for a given parameter set. The EC luminosity is treated following prescriptions for anisotropic radiation fields in the reference frame of the emitting region (see Dermer et al. 1992; Sikora et al. 1994; Dermer 1995; Stawarz et al. 2003).

In order to reduce the number of free parameters in the model, we linked together or fixed some of the quantities (see Table 1). The height of the emitting knot z_d is equal to the jet linear size, measured from the core to the jet termination (hereafter LS).

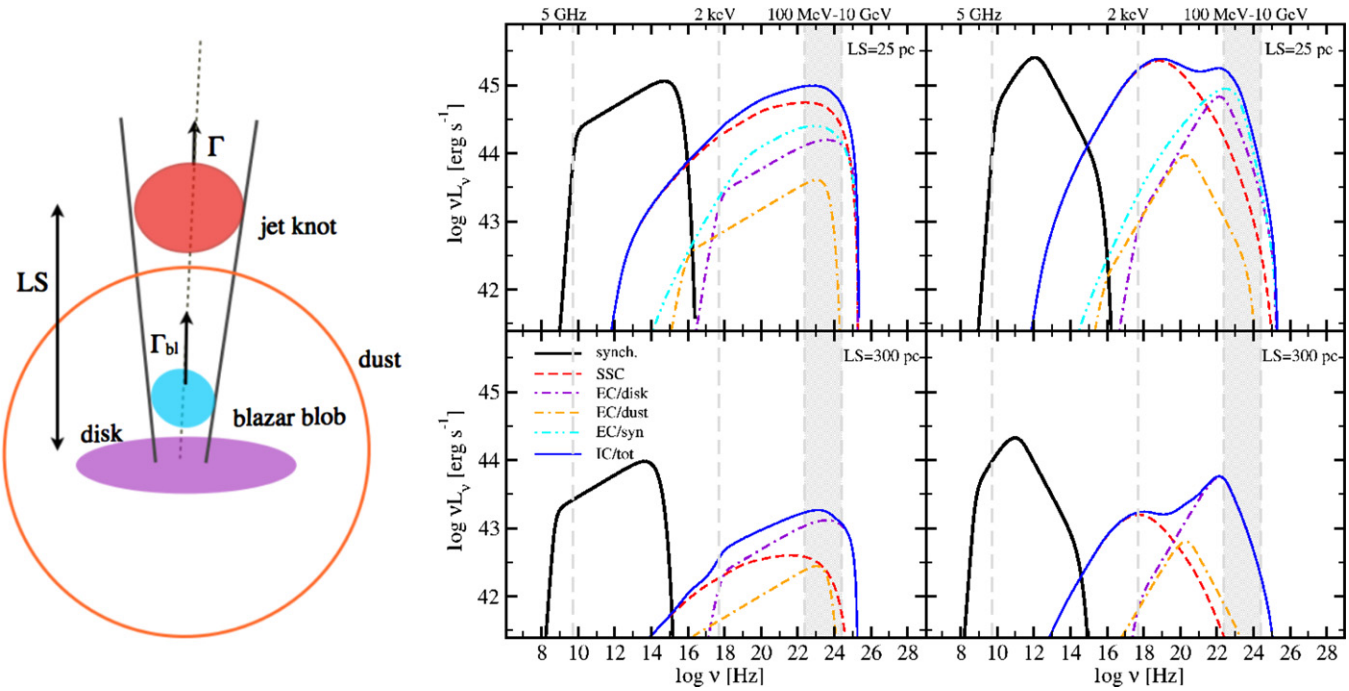

Figure 1. Left: illustration of the jet model: the observed jet luminosities are produced in a jet spherical knot (in red). The external photon fields contributing to the jet EC emission are schematically illustrated: the disk, dust, and blazar component at the base of the jet (in cyan). Right: simulated SED for a 25 pc jet (upper panels) and a 300 pc jet (lower panels). The jet parameters are: $L_{\rm jet,kin} = L_{\rm disk} = 10^{46}$ erg s^{-1}, $\Gamma = 2.0$, $\theta = 30^{\circ}$. Left panels: the assumed EED is a simple power law with $\gamma_{\rm min} = 10$, $\gamma_{\rm max} = 10^5$, p = 2.68. Right panels: the assumed EED is a broken power law with $\gamma_{\rm min} = 10$, $\gamma_{\rm max} = 10^5$, $\gamma_{\rm break} = 2 \times 10^3$, p = 2.1, p2 = 4.0. Note that the EC/syn component is not included in the SED of the 300 pc jet (see the text).

(A color version of this figure is available in the online journal.)

Table 1
Model Parameters

Notation	Definition	Value/Range
	Free Input Parameters	
LS	Jet LS (core to jet termination)	10 pc–10 kpc
$L_{\rm disk}$	Bolometric disk luminosity	10^{45}–10^{47} erg s^{-1}
Γ	Jet knot bulk Lorentz factor	1.4–10
θ	Observer's viewing angle	10°–50°
	Linked Parameters	
R	Knot radius	0.1LS
z_d	Knot distance from the BH	LS
$L_{\rm jet,kin}$	Jet kinetic power	$(0.01, 0.1, 1.0)L_{\rm disk}$
U'_e	Radiating EED	$\propto L_{\rm jet,kin}$
U'_B	Magnetic field energy density	$U_e/U_B = 10$
$L_{\rm dust}$	Dust/IR luminosity	$0.1L_{\rm disk}$
$R_{\rm dust}$	Dust shell radius	$\propto \sqrt{L_{\rm disk}}$
$L_{\rm bl}$	Synchrotron radiative power of the blazar-like blob	$10\%L_{\rm jet,kin}$
	Fixed Parameters	
$\gamma_{\rm min}$	Minimum electron Lorentz factor	10
$\gamma_{\rm max}$	Maximum electron Lorentz factor	10^5
$\gamma_{\rm break}$	Energy break Lorentz factor (broken power law)	2×10^3
p	EED index (single power law)	2.68
	EED low energy index (broken power law)	2.1
$p2$	EED high energy index (broken power law)	4.0
$T_{\rm disk}$	Disk blackbody temperature	3×10^4 K
$T_{\rm dust}$	Dust blackbody temperature	370 K
$\Gamma_{\rm bl}$	Blazar-like blob bulk Lorentz factor	10

The jet has a conical geometry with a semi-aperture angle equal to 0.1 ($R = 0.1$LS), which allows for reasonable sizes of the knot radius R (1 pc to 1 kpc) within the considered linear scales (LS $\leqslant$ 10 kpc).

The fraction of disk photons reprocessed by nuclear dust in a putative torus is fixed to $L_{\rm dust} = 0.1L_{\rm disk}$, in agreement with luminosities found for type 1 quasars (Hatziminaoglou et al. 2008), where the disk emission can be directly observed. Since we are not aiming at a detailed model of the source spectrum, the thermal emission from the disk and the dust is simply modeled with a blackbody spectrum. We set the disk temperature $T_{\rm disk}$ to $\sim 3 \times 10^4$ K. The dust temperature ($T_{\rm dust} \sim$ 370 K) is derived from the observed peak frequency of the IR emission ($\nu_{\rm dust} = 3 \times 10^{13}$ Hz Cleary et al. 2007) using the formula $T_{\rm dust} = h\nu_{\rm dust}/(3.93k)$ (see Ghisellini & Tavecchio 2009). The considered spatial scales are larger than 1 pc, thus we always treat the disk as a point-like source of photons, with the energy density[10] of the disk photons, $U'_{\rm disk}$, scaling as $1/{\rm LS}^2$ (and $1/\Gamma^2$). For simplicity, we assumed a thin spherical shell for the dust spatial distribution, the shell radius being $R_{\rm dust} = 2.5 \times 10^{18}\sqrt{L_{\rm disk}/10^{45}}$ cm (Błażejowski et al. 2000; Sikora et al. 2002). The dust photon energy density, $U'_{\rm dust}$, is computed using Equation 21 in Ghisellini & Tavecchio (2009) when $z_d < R_{\rm dust}$ and considering a point-like source of photons when $z_d > R_{\rm dust}$. The value of $U'_{\rm dust}$ at the discontinuity point, $z_d = R_{\rm dust}$, is the average between the dust energy densities immediately inside and outside the shell.

We assume a link between the accretion and ejection processes related to the supermassive BH. The power carried by the jet in radiating particles and the Poynting flux ($L_{\rm jet,kin}$) is proportional to the disk luminosity, $L_{\rm disk}$. A relation between the jet and disk powers in extragalactic radio sources has been considered by Rawlings & Saunders (1991), who found that the average jet kinetic power, necessary to support the radio

[10] Hereafter, primed energy densities and luminosities are in the jet knot comoving frame.

lobes, is comparable with the accretion disk luminosity. In powerful blazars, an energetically dominant proton component is required to account for the radiative jet luminosities and the jet total power can be even larger than the accretion disk luminosity ($L_{\rm jet,kin}/L_{\rm disk} = 1.0$–$10$ Celotti & Ghisellini 2008; Ghisellini et al. 2010). In GPS radio galaxies, Ostorero et al. (2010) inferred $L_{\rm jet,kin}/L_{\rm disk} = 0.01$–$0.1$ based on their modeling of the lobe emission.

We set the parameters of the blazar-like blob referring to the estimated ranges of the sample of Flat Spectrum Radio Quasars (FSRQs; Celotti & Ghisellini 2008): the blazar blob emits 10% of the jet kinetic power via synchrotron emission and has a bulk motion of $\Gamma_{\rm bl} = 10$.

To summarize, in the model LS, $L_{\rm disk}$, Γ and the observers viewing angle θ are free input parameters, z_d is equal to LS, and the jet kinetic power $L_{\rm jet,kin}$ and the dust emission $L_{\rm dust}$ are both proportional to $L_{\rm disk}$. In addition, we assume a moderate dominance of particles over the magnetic field energy density in the knot: $U'_e/U'_B = 10$, where U'_e is the energy density of the radiating electrons and U'_B is the magnetic field energy density, respectively. Observations indicate that radio lobes in young sources are in equipartition conditions (see Orienti & Dallacasa 2008). However, in jet knots of FRII radio galaxies, radio and X-ray observations point to intensities of the magnetic field below the values expected under the assumption of energy equipartition with the radiating particles, when the X-ray emission is ascribed to IC emission (see, e.g., Kataoka & Stawarz 2005). Similarly, SED modeling of multiwavelength emission of FSRQ and BL Lac objects points to particle-dominated jets (Celotti & Ghisellini 2008).

We allow the shape of the electron energy distribution (hereafter EED) to be either a simple power law, $N(\gamma) = k_e\gamma^{-p}$, or a broken power law. The minimum and maximum electron Lorentz factor, $\gamma_{\rm min}$ and $\gamma_{\rm max}$, are fixed to 10 and 10^5, respectively. The parameter values of the EED ($p = 2.68$ for the single power-law spectral index; $p = 2.1$ and $p2 = 4.0$ and $\gamma_{\rm break} \sim 2 \times 10^3$ for the spectral indices of the broken power law and the energy break, respectively) are derived from observations, as discussed in the following section. The model parameters (and the assumed values) are listed in Table 1.

3. SIMULATED JET SED

We simulate the jets' SED for a range of LS and bolometric disk luminosities, $L_{\rm disk}$. Our simulations cover the range of LS and $L_{\rm disk}$ values of the sample of young radio quasars with an X-ray detection presented in Siemiginowska et al. (2008), LS = 0.01–10 kpc and $L_{\rm disk} = 10^{45}$–10^{47} erg s^{-1} ,respectively. In fact, we anticipate that X-rays provide important constraints on the model-predicted γ-ray luminosities. The optical–UV emission of the GPS and CSS quasars displays the typical features of broad-line quasars, with a detected UV bump and broad emission lines, and the measured intrinsic absorption columns in the X-rays are less than a few $\times 10^{21}$ cm^{-2} (Siemiginowska et al. 2008). Thus, we do not expect the disk emission to be heavily affected by obscuration. Since the observed disk emission is not modified by other orientation effects, e.g., relativistic beaming, we use it to define the luminosity range of our simulations.

Mildly to highly relativistic jet velocities are considered, with values of the bulk motion Γ between 1.4 and 10, where the minimum value refers to the study presented in Mullin & Hardcastle (2009). We allowed observer's viewing angles, θ, in the 10° to 50° range so that we exclude the most closely aligned objects (i.e., blazar sources). Inclination angles $\lesssim 10°$ would also imply larger jet LSs for the quasars in the sample than typical GPS and CSS sources. It is, however, true that single components within the jet (i.e., a single knot or the inner jet) might have smaller θ.

The shape of the EED in young sources is not well known. Here, we consider a single and a broken power law. The spectral index for the single power-law EED is set to the median X-ray photon index ($\Gamma_X = 1.84 \pm 0.24$, $p = 2\Gamma_X - 1$) of the sample of GPS and CSS quasars (Siemiginowska et al. 2008). In the broken power-law EED, we set the spectral index below and above the energy break to $p = 2.1$ and $p2 = 4.0$, respectively. The low-energy index is consistent (within the errors) with the average Γ_X in radio loud quasars ($\Gamma_X = 1.57 \pm 0.08$ and $\Gamma_X = 1.55 \pm 0.17$, Bechtold et al. 1994; Belsole et al. 2006, respectively). We refer to γ-ray observations of misaligned radio sources to derive the spectral index above the energy break: we consider the sample of misaligned radio sources detected by *Fermi*-LAT and select the central value in the range of their measured γ-ray photon indices ($\Gamma_\gamma \sim 1.9$–3.0; Abdo et al. 2010b; Kataoka et al. 2011; Ackermann et al. 2012). The energy break is fixed to an intermediate value between the minimum and maximum electron Lorentz factor, $\gamma_{\rm break} \sim 2 \times 10^3$. Similar EED functions have been inferred by modeling the broadband SED of hot spots (see the cases of Cygnus A, PKS 1421-490, and 3C 445 in Stawarz et al. 2007; Godfrey et al. 2009; Perlman et al. 2010, respectively) and blazar jets (Celotti & Ghisellini 2008; Ghisellini & Tavecchio 2009; Sikora et al. 2009). In this work, we do not discuss a specific theoretical scenario for the particle acceleration process. However, it is interesting to note that, in jets, indications for electron injection spectra that deviate from the standard E^{-2} form (related to first-order Fermi acceleration process in non-relativistic shocks) come from observations (Stawarz et al. 2007; Godfrey et al. 2009; Perlman et al. 2010; Celotti & Ghisellini 2008; Ghisellini & Tavecchio 2009; Sikora et al. 2009) and simulations (see, e.g., the results of particle in cell simulations presented in Sironi & Spitkovsky 2011 and references therein).

We allow three jet-to-disk power ratios, $L_{\rm jet,kin}/L_{\rm disk} = 0.01$, 0.1, and 1.0, hence, given the assumed $L_{\rm disk}$ values, the minimum and maximum jet powers in our simulations are 10^{43} and 10^{47} erg s^{-1}, respectively. These values cover the ratios previously inferred for radio sources, including GPS radio galaxies (e.g., Ostorero et al. 2010). We do not consider the case of $L_{\rm jet,kin}/L_{\rm disk} > 1$, which was derived for FSRQs and could be possibly associated with flaring states limited in time (see Celotti & Ghisellini 2008; Abdo et al. 2010a; Tanaka et al. 2011 and references therein for a discussion).

In Figure 1, we show the simulated SED for a jet with $L_{\rm jet,kin} = L_{\rm disk} = 10^{46}$ erg s^{-1}, moving with $\Gamma = 2.0$ and observed at $\theta = 30°$. The SED are for two considered LSs, LS = 25 pc (upper panels) and LS = 300 pc (lower panels), and for the two assumed functions of the EED (the single power law in the left panels and the broken power law in right panels).

The low-energy part of the spectrum includes synchrotron self-absorption effects. The characteristic convex spectral shape observed at radio frequencies in young sources could also be due to free–free absorption by an inhomogeneous ambient medium. However, such an effect is likely to be more important in the radio lobes' synchrotron spectrum (see Bicknell et al. 1997; Begelman 1999; Stawarz et al. 2008).

For the single power-law EED, the SED of the 25 pc jet above $\sim 10^{16}$ Hz is dominated by one mechanism, i.e., SSC radiation. For the same LS, in the broken power-law case the

X-ray luminosity (and up to $\approx 10^{21}$ Hz) is mainly produced via SSC while the γ-ray luminosity ($\sim 10^{22}$–10^{24} Hz) is produced via EC/syn. The energy density of the synchrotron photons produced by the blazar-like component scales as $\Gamma_{\rm bl}^4/\Gamma^2 \times 1/z_d^2$ (in the knot rest frame; see Celotti et al. 2001; Migliori et al. 2012). Therefore, the EC/syn luminosity is expected to be intense in powerful jets that decelerate on scales of tens of pc. In misaligned sources (e.g., $\gtrsim 20^\circ$ for our model parameters), such a component can be brighter than the high-energy emission from the inner blazar component.

The underlying EED shape determines the observed X-ray to γ-ray spectrum, with a slope of the SED (for the 25 pc jet) that is steep for the single power-law EED and flat for the broken power law. The difference between the two SED holds true even when the EC/syn component is not present. In fact, the EC/disk luminosity peaks in the γ-ray band and still dominates over the SSC γ-ray emission in the broken power-law EED case.

The radiative output of the jet decreases at all wavelengths for increasing LS. Furthermore, the dominant contributions to the X-ray and γ-ray bands may change as the source expands. Figure 1 shows that the EC/disk luminosity dominates the high-energy output of the 300 pc jet. This follows from the model scaling relations for the synchrotron and IC luminosities. Given the jet kinetic power in radiating particles and magnetic field:

$$L_{\rm jet,kin} \approx \pi R^2 c \Gamma^2 (U'_e + U'_B) \approx 10^{-3} \pi c {\rm LS}^2 \Gamma^2 U'_e, \quad (1)$$

where $U'_e = 10\, U'_B$ and $R = 0.1$ LS, the total synchrotron luminosity in the jet comoving frame depends on the jet power and the volume of the emitting region:

$$L'_{\rm syn} \propto U'_e U'_B V \propto L_{\rm jet,kin}^2 {\rm LS}^{-1} \Gamma^{-4}. \quad (2)$$

The EC luminosities related to the disk emission (EC/disk, EC/dust) scale in the same way (for $z_d = {\rm LS}$):

$$L'_{\rm EC} \propto U'_e U'_{\rm disk/dust} V \propto L_{\rm jet,kin}^2 {\rm LS}^{-1} \Gamma^{-4}, \quad (3)$$

for $L_{\rm jet,kin} \propto L_{\rm disk}$ and $z_d > R_{\rm dust}$, i.e., when the emitting knot is out of the torus region (for $z_d \lesssim R_{\rm dust}$: $L'_{\rm EC/dust} \propto \Gamma^0$), while the SSC luminosity scales as

$$L'_{\rm SSC} \propto U'_e U'_{\rm syn} V \propto L_{\rm jet,kin}^3 {\rm LS}^{-2} \Gamma^{-6}, \quad (4)$$

where $U'_{\rm syn}$ is the energy density of the synchrotron photons in the jet/knot rest frame.

The SSC luminosity decreases faster than EC luminosities with LS. This is evident in the SED for the 300 pc jet: for both assumed EEDs, the EC/disk luminosity peak is higher than the SSC one. Interestingly, in the broken power-law EED this also changes the X-to-γ-ray luminosity ratio (and slope) with respect to the SED of the 25 pc jet. Note that the EC/syn component is not considered at LS = 300 pc, as it becomes fainter than the blazar emission.

3.1. Simulated Gamma-Ray Luminosity Distributions

For each of the simulated SEDs, we computed the synchrotron luminosity at 5 GHz ($L_{\rm 5\,GHz}$), the X-ray luminosity at 2 keV ($L_{\rm 2\,keV}$), and the integrated 100 MeV–10 GeV luminosity ($L_{\rm 100\,MeV-10\,GeV}$) in the observers rest frame. The 2 keV and 100 MeV–10 GeV luminosities are obtained by adding up all the IC contributions (SSC, EC/disk, EC/dust, and EC/syn) at each frequency. For the assumed jet parameter ranges, the synchrotron emission never significantly contributes at 2 keV. We recall that the external Compton emission on the blazar-like synchrotron photons (EC/syn) is included only when, for a given parameter set, it is larger than the estimated high-energy emission of the blazar component itself, assuming for the latter SSC and IC on the broadline and dusty torus photons. This happens in $\sim$10% of the cases for the simulated distributions.

Figure 2 shows the γ-ray luminosity of the simulated jets as a function of their radio ($L_{\rm 5\,GHz}$–$L_{\rm 100\,MeV-10\,GeV}$, upper panels) and X-ray luminosities ($L_{\rm 2\,keV}$–$L_{\rm 100\,MeV-10\,GeV}$, lower panels), for the two considered EED (left and right panels for the single and the broken power-law EED, respectively) and jet-to-disk power ratios ($L_{\rm jet,kin}/L_{\rm disk} = 0.01$, 0.1 and 1.0).

Figure 3 illustrates how the input model parameters, $L_{\rm jet,kin}$, LS, Γ, and θ, shape the simulated $L_{\rm 5\,GHz}$ –$L_{\rm 100\,MeV-10\,GeV}$ distributions. We use the $L_{\rm jet,kin}/L_{\rm disk}$ =1.0 distribution (in the single power-law EED case) as an example: each trail in the figure highlights the path in luminosity–luminosity space when varying a single input parameter while keeping the others fixed.

Powerful ($L_{\rm jet,kin} \sim 10^{47}$ erg s^{-1}) and small (LS $\sim$ 10 pc) sources are the most intrinsically luminous, while low power and large (LS $\sim$ 10 kpc) sources are the least intrinsically luminous, as expected from the scalings of the luminosities in Equations (2)–(4). Effects related to the jet speed, the orientation with respect to the line of sight, and the selected monochromatic luminosities (in the observers rest frame) are also important. Modifications of the emitted luminosities in the observers rest frame due to θ and Γ are expressed via the Doppler factor δ ($\delta = 1/(\Gamma - \sqrt{\Gamma^2 - 1} \times \cos\theta)$). The intrinsic luminosity transforms in the observers frame as $\nu L_\nu \sim \nu L'_\nu \delta^4$ and the observed luminosity of a jet may change by orders of magnitude for increasing θ depending on its bulk motion. For $\Gamma = 10$, for instance, δ changes from $\sim$5 to $\sim$0.3 going from $\theta = 10^\circ$ to $\theta = 50^\circ$, with a corresponding variation of more than four orders of magnitude in $L_{\rm 5\,GHz}$ and $L_{\rm 100\,MeV-10\,GeV}$. The position of a jet (with a given set of LS, $L_{\rm jet,kin}$, and Γ) can therefore migrate across the $L_{\rm 5\,GHz}$ ($L_{\rm 2\,keV}$)–$L_{\rm 100\,MeV-10\,GeV}$ space depending on θ (see Figure 3). Doppler effects may be particularly relevant for monochromatic (or band) luminosities close to the extremes of the synchrotron and IC spectra, where even a small shift along the frequency axis ($\nu = \nu'\delta$, where ν' and ν are the emitted and observed frequency, respectively) significantly changes the observed luminosity.

The $L_{\rm 5\,GHz}$ –$L_{\rm 100\,MeV-10\,GeV}$ distributions (and the $L_{\rm 5\,GHz}$ –$L_{\rm 2\,keV}$ distributions in Figure 4) present a fan-like shape, with an increasing spread of the $L_{\rm 5\,GHz}$ –$L_{\rm 100\,MeV-10\,GeV}$ relation for $L_{\rm 5\,GHz} \gtrsim 10^{42}$ erg s^{-1}. In intrinsically powerful sources, $L_{\rm 5\,GHz}$ drastically increases when the jet (and therefore the volume of the emitting region) expands up to a few hundred pc and the 5 GHz frequency shifts from the optically thick to the optically thin part of the synchrotron spectrum. For LS $\gtrsim$ 100 pc, $L_{\rm 5\,GHz}$ progressively declines (following $L'_{\rm syn} \propto {\rm LS}^{-1}$), as shown in Figure 3. In low-luminosity sources, the turn-over frequency from the optically thick to the optically thin regime is below 5 GHz at all the considered LSs, thus $L_{\rm 5\,GHz}$ simply declines $\propto {\rm LS}^{-1}$ (when all the other input parameters are fixed). This explains the fact that for lower jet power intervals (i.e., when $L_{\rm jet,kin}/L_{\rm disk} = 0.01$ is assumed), the $L_{\rm 5\,GHz}$–$L_{\rm 100\,MeV-10\,GeV}$ distributions are more linear, although with dispersion.

For decreasing $L_{\rm jet,kin}/L_{\rm disk}$, the whole $L_{\rm 5\,GHz}$ –$L_{\rm 100\,MeV-10\,GeV}$ distribution shifts to lower radio and γ-ray maximum and minimum luminosities. Interestingly, jets with $L_{\rm jet,kin}/L_{\rm disk}$ =

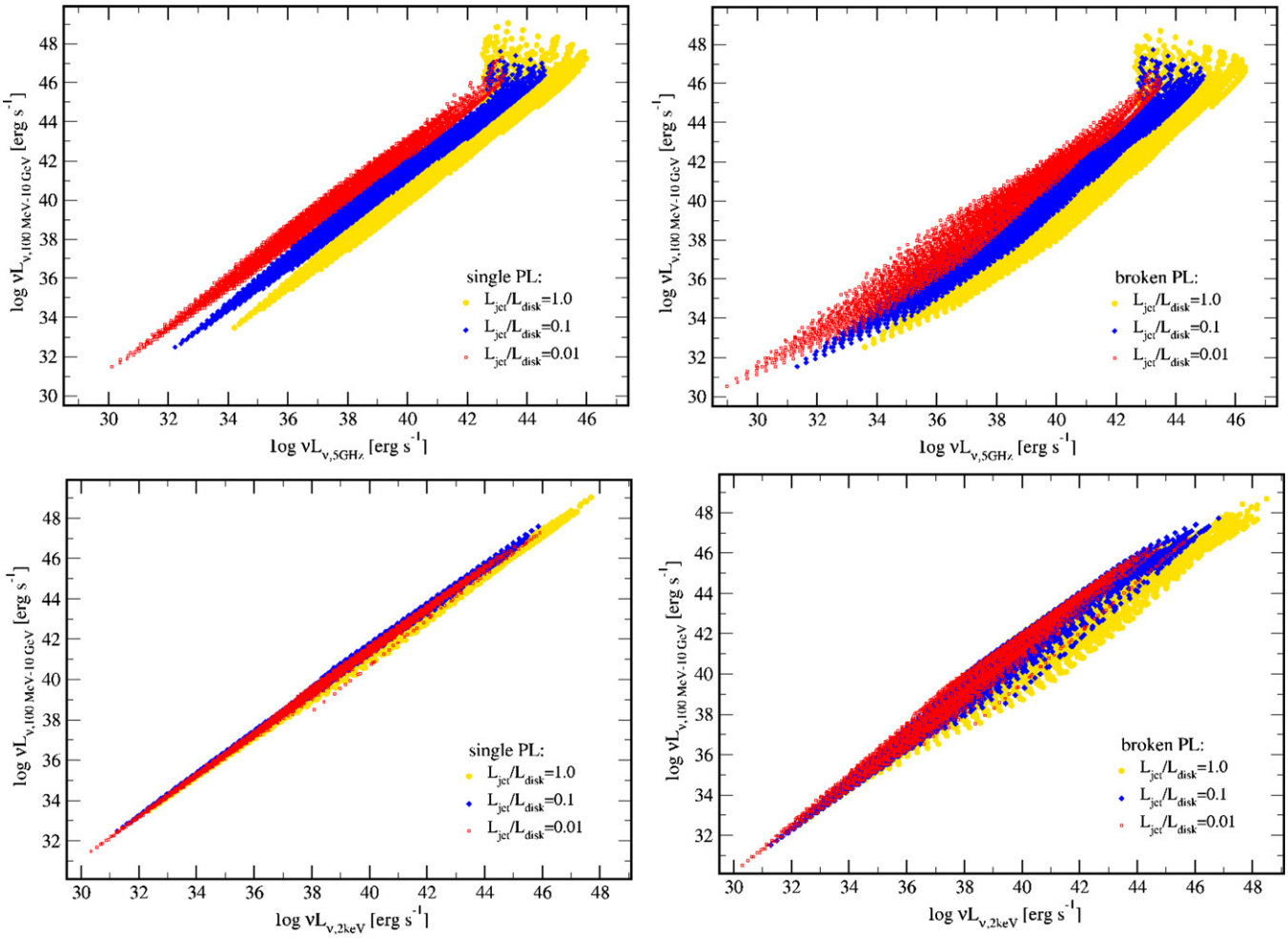

Figure 2. γ-ray (100 MeV–10 GeV) luminosities are plotted as a function of the radio (5 GHz, upper panels) and X-ray (2 keV, lower panels) luminosities for the simulated jets. All luminosities are calculated in the observer's reference frame. The simulated jets cover a range of LSs (10 pc–10 kpc), bulk Lorentz factors ($\Gamma = 1.4$–10), and observer viewing angles ($\theta = 10^\circ$ –50°). The yellow solid circles are the simulated sources assuming $L_{\rm jet,kin} = L_{\rm disk}$, the blue solid diamonds are the simulated sources for $L_{\rm jet,kin} = 0.1 L_{\rm disk}$, and the red empty squares are for $L_{\rm jet,kin} = 0.01 L_{\rm disk}$. The (bolometric) disk luminosities $L_{\rm disk}$ are in the range 10^{45}–10^{47} erg s^{-1}. The left panels show simulations for a single power-law EED with $p = 2.68$ and the right panel shows a broken power law with $p = 2.1$, $p2 = 4.0$, and $\gamma_{\rm break} = 2 \times 10^3$. In the EED, the minimum and maximum random Lorentz factors are $\gamma_{\rm min} = 10$ and $\gamma_{\rm max} = 10^5$, respectively.

(A color version of this figure is available in the online journal.)

0.01 can still be relatively γ-ray luminous ($L_{100\,\rm MeV-10\,GeV} \sim 10^{46}$–$10^{47}$ erg s^{-1}). We also note that, for a fixed $L_{5\,\rm GHz}$, the highest $L_{100\,\rm MeV-10\,GeV}$ are obtained for the smallest jet-to-disk ratio ($L_{\rm jet,kin}/L_{\rm disk} = 0.01$). This is due to the fact that EC/disk provides the dominant contribution in the γ-ray band. Finally, the $L_{5\,\rm GHz} - L_{100\,\rm MeV-10\,GeV}$ relation shows a lower dispersion for the single power-law EED than for the broken power-law EED, as expected for a simpler spectral shape.

The simulated $L_{100\,\rm MeV-10\,GeV} - L_{2\,\rm keV}$ distributions (Figure 2, lower panels) are linear for all the considered $L_{\rm jet,kin}/L_{\rm disk}$; due to the fact that the X-ray and γ-ray emission is produced by the same electron population via the IC mechanism. The distributions obtained from the broken power-law EED have a larger dispersion than the simple power-law EED. In fact, in the former case, $L_{2\,\rm keV}$ and $L_{100\,\rm MeV-10\,GeV}$ can be related to different IC emission, e.g., SSC emission in the X-rays and EC in the γ-rays (as in the example in Figure 1). A dominant SSC contribution in the X-rays is expected in powerful and small jets ($L_{\rm jet,kin} \sim 10^{46}$–$10^{47}$ erg s^{-1}, LS $\sim$ 10 pc), since $L'_{\rm SSC} \propto L^3_{\rm jet,kin} {\rm LS}^{-2}$. For $L_{\rm jet,kin}/L_{\rm disk} = 0.01$ and 0.1, the relative increase of EC/disk and EC/dust over SSC in the X-ray band reduces the spread of the $L_{2\,\rm keV}$–$L_{100\,\rm MeV-10\,GeV}$ distribution with respect to the $L_{\rm jet,kin}/L_{\rm disk} = 1.0$ case. In addition, in the γ-ray band, attenuation of the IC flux may happen when the scattering occurs in the Klein–Nishina regime (which is included in the model computation of the IC spectrum).

3.2. $L_{5\,GHz}$, $L_{2\,keV}$, $L_{100\,MeV-10\,GeV}$ Relation

The simulated $L_{5\,\rm GHz}$–$L_{100\,\rm MeV-10\,GeV}$ and $L_{2\,\rm keV}$–$L_{100\,\rm MeV-10\,GeV}$ luminosity distributions provide indications to select candidates for a γ-ray detection, based on radio and X-ray luminosities. The radio luminosity ($L_{5\,\rm GHz}$) alone is not a sufficient selection criterion, in particular for sources with a dominant, luminous ($L_{5\,\rm GHz} \gtrsim 10^{42}$ erg s^{-1}) jet component. In fact, for a selected $L_{5\,\rm GHz}$ luminosity in the $\sim 10^{42}$–10^{44} erg s^{-1} interval, the corresponding allowed γ-ray luminosities span between $\sim 10^{43}$–10^{48} erg s^{-1}. When $L_{5\,\rm GHz} \lesssim 10^{42}$ erg s^{-1}, the γ-ray luminosities are constrained within an interval of $\sim$1–2 orders of magnitude. The $L_{2\,\rm keV}$–$L_{100\,\rm MeV-10\,GeV}$ distribution has a constant linearity over several orders of magnitude. Nevertheless, radio observations are certainly needed: classification of young

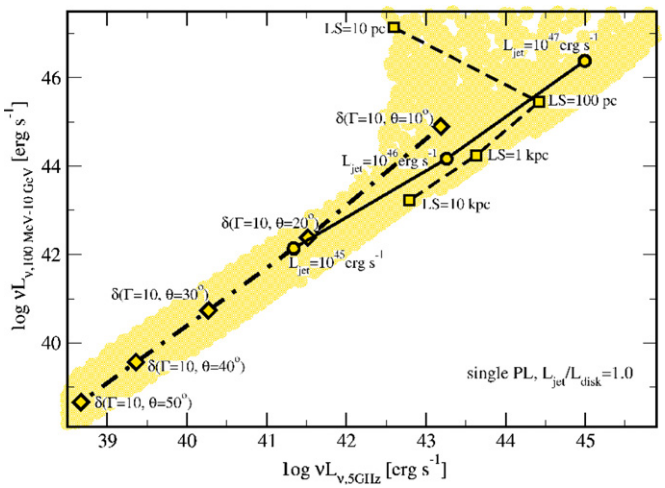

Figure 3. Dependencies of the simulated distribution (for the case of $L_{\rm jet,kin} = L_{\rm disk}$ and a single power-law EED) on the free parameters are highlighted. Each trail shows how the position of a source changes in the $L_{5\,\rm GHz}$ –$L_{100\,\rm MeV-10\,GeV}$ plot for a single varying parameter. The solid black line connecting the circles shows the evolution as a function of the jet power for a source with LS = 100 pc, $\Gamma = 4$, and $\theta = 20^{\circ}$. The dashed line and squares show the evolution with LS for a source with $L_{\rm jet,kin} = 10^{46}$ erg s^{-1}, $\Gamma = 1.4$, and $\theta = 20^{\circ}$. The dot-dashed line and diamonds show the effect of a beaming factor (varying θ and leaving Γ fixed) for a source with $L_{\rm jet,kin} = 10^{46}$ erg s^{-1} and LS = 10 pc.

(A color version of this figure is available in the online journal.)

radio sources rely on radio observations, which allow us to probe smaller scales than X-rays and to resolve different radio components.

We used the simulated luminosity distributions to derive relations among the three luminosities, $L_{5\,\rm GHz}$, $L_{2\,\rm keV}$, and $L_{100\,\rm MeV-10\,GeV}$, for the considered jet-to-disk ratios and EEDs. A fit of the simulated data applying a linear model, with the coefficients estimated by the least-squares method, returned the following relations for the $L_{\rm jet,kin}/L_{\rm disk}$ =1.0 distribution in the case of the single power-law EED:

$$\mathrm{Log}L_{100\,\rm MeV-10\,GeV,44} = 1.34 + 0.09 \times \mathrm{Log}\,L_{5\,\rm GHz,44} + 0.94 \times \mathrm{Log}L_{2\,\rm keV,44}, \quad (5)$$

and the broken power-law EED:

$$\mathrm{Log}L_{100\,\rm MeV-10\,GeV,44} = 0.62 + 0.48 \times \mathrm{Log}\,L_{5\,\rm GHz,44} + 0.64 \times \mathrm{Log}L_{2\,\rm keV,44}, \quad (6)$$

with all the luminosities in units of 10^{44} erg s^{-1}. The scatter in $L_{100\,\rm MeV-10\,GeV}$ at fixed $L_{5\,\rm GHz}$ and $L_{2\,\rm keV}$ is 0.16 dex and 0.55 dex for Equations (5) and (6), respectively. Note that this scatter is derived only from our jet model.

The coefficients of the best fit and relative dispersion for all the simulated distributions are reported in Table 2. We emphasize that these relations are indicative of the expected γ-ray luminosities for the assumed jet model and assigned ranges of the parameters.

Table 2
Results of the Least-squares Model Fit for the $L_{5\,\rm GHz}$-$L_{2\,\rm keV}$-$L_{100\,\rm MeV-10\,GeV}$ Simulations

Simulations		Best Fit			
$L_{\rm jet,kin}/L_{\rm disk}$	EED	x0	x1	x2	Disp.
(1)	(2)	(3)	(4)	(5)	(6)
1.0	SP	1.34	0.09	0.94	0.16
	BP	0.62	0.48	0.64	0.55
0.1	SP	1.63	0.05	0.99	0.10
	BP	1.51	0.41	0.72	0.40
0.01	SP	1.68	0.07	0.97	0.12
	BP	1.02	0.21	0.91	0.40

Notes. Columns: 1: assumed jet-to-disk ratio; 2: shape of the EED: SP = single power law, BP = broken power law; 3: intercept ($L_{100\,\rm MeV-10\,GeV}$ are in units of 10^{44} erg s^{-1}); 4: $L_{\rm 5GHz,44}$ coefficient; 5: $L_{\rm 2keV,44}$ coefficient; 6: intrinsic dispersion.

4. X-RAY YOUNG SOURCES SAMPLE

4.1. Predicted γ-Ray Fluxes

In order to search for jet-related γ-ray emission in young radio sources, we selected a sample requiring that (1) all the sources have radio and X-ray observations and (2) the jet is likely the most relevant contribution to the non-thermal emission. We considered GPS and CSS radio quasars (Stanghellini et al. 2001), since in young radio galaxies the compact radio lobes could dominate the non-thermal contribution (Stawarz et al. 2008; Ostorero et al. 2010). Our sample is composed of 13 quasars, 6 classified as GPS sources, and 7 classified as CSS sources. All the sources were part of a dedicated X-ray study with *Chandra* observations. The results of the X-ray analysis were presented in Siemiginowska et al. (2008). In Table 3, we report the redshift, estimated projected size, radio (5 GHz), X-ray (2 keV), and estimated bolometric ($L_{\rm bol}$) luminosities of the sample. The sample, although not complete by any means, is the largest sample available of GPS and CSS quasars with X-ray (and radio) observations.

Before proceeding further, we comment on the nature of GPS quasars. It is known that GPS quasar samples are partly contaminated by quasars with a core-jet structure that appears compact only because of projection effects. Stanghellini et al. (2005) found that large-scale emission, indicative of the presence of an extended structure, is often detected in GPS quasars. Even though young quasars could display some degree of radio fluctuations, radio variability gives a definite clue for an aligned quasar, i.e., one with a blazar-like nature (see Tinti et al. 2005). An example is the case of PKS 1127-14, which was initially classified as a GPS quasar. X-ray and radio observations have revealed the presence of a kpc-scale jet (Siemiginowska et al. 2002, 2007). This, together with the observed multi-band flux variability and superluminal expansion of the core region, points to a blazar nature of the source (Błażejowski et al. 2004). We still included this source in our sample for comparison with the other GPS/CSS quasars.

In Figure 4, we plot the $L_{2\,\rm keV}$ of the quasars in the sample as a function of their $L_{5\,\rm GHz}$ and compare them with the simulated distributions. Here, we have simply ascribed all the 5 GHz luminosity to the jet. This approximation is more risky in the case of GPS than CSS sources, because the synchrotron emission of the GPS compact ($\lesssim$1 kpc) lobes could be important in the GHz band. We have also assumed that the bulk of the 2 keV flux is produced by the jet. This hypothesis is indeed part of the jet scenario that we want to probe by comparing model predictions with observations.

The quasars occupy the high-luminosity region of the $L_{5\,\rm GHz}$–$L_{2\,\rm keV}$ plot. This regime is well sampled by our simulations when $L_{\rm jet,kin}/L_{\rm disk}$ =1.0 (for both assumed EEDs), while the overlap with the $L_{\rm jet,kin}/L_{\rm disk} = 0.01$ distribution is only marginal. A significant overestimate of the $L_{5\,\rm GHz}$ of the

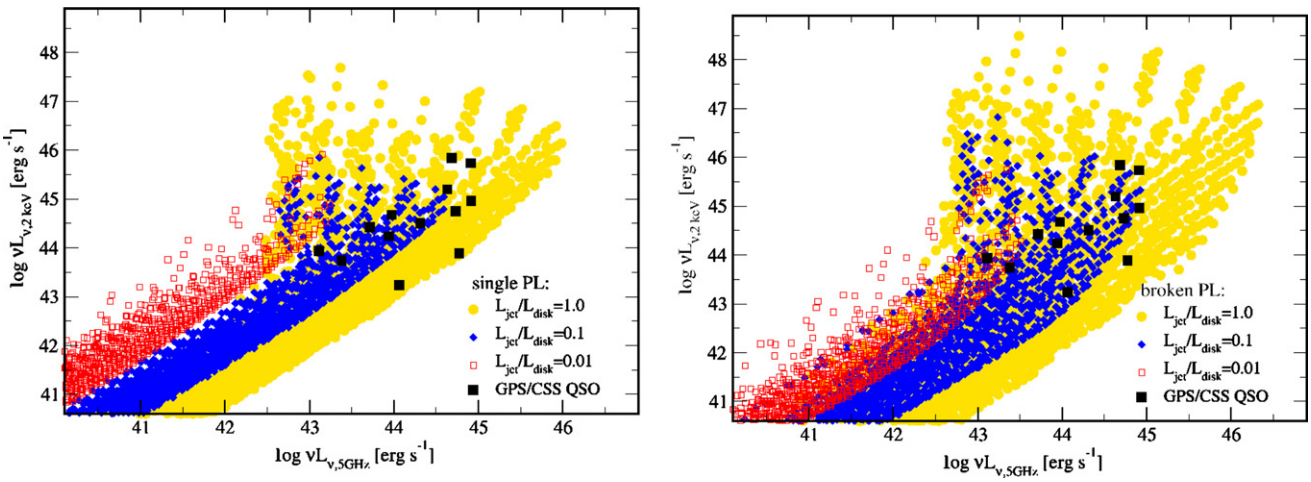

Figure 4. X-ray luminosities $L_{2\,\mathrm{keV}}$ of the GPS and CSS quasars (Table 3) and the simulated sources as a function of radio luminosities $L_{5\,\mathrm{GHz}}$ (observers rest frame): the yellow solid circles are the simulated sources assuming $L_{\mathrm{jet,kin}} = L_{\mathrm{disk}}$, the blue solid diamonds are the simulated sources for $L_{\mathrm{jet,kin}} = 0.1L_{\mathrm{disk}}$, and the red empty squares are for $L_{\mathrm{jet,kin}} = 0.01L_{\mathrm{disk}}$. The black solid squares are the GPS and CSS quasars.

(A color version of this figure is available in the online journal.)

Table 3
The Sample of GPS/CSS Quasars with *Chandra* Observations in Siemiginowska et al. (2008)

Source	Type	z	LS (pc)	$\log(L_{5\,\mathrm{GHz}})$ (erg s^{-1})	$\log(L_{2\,\mathrm{keV}})$ (erg s^{-1})	$\log(L_{\mathrm{bol}})$ (erg s^{-1})	$\log(L_{100-10,\mathrm{SPL}})^{a}/\log(L_{100-10,\mathrm{BPL}})^{b}$ (erg s^{-1})
(1)	(2)	(3)	(4)	(5)	(6)	(7)	(8)
Q0134+329/3C 48	CSS	0.367	1.27×10^3	43.97	44.68	45.96	45.98/45.04
Q0615+820	GPS	0.71	1.80×10^3	43.94	44.23	45.37	45.56/44.74
Q0740+380/3C 186	CSS	1.063	10×10^3	43.72	44.42	46.02	45.71/44.75
Q0741+311	GPS	0.63	30	44.31	44.51	45.11	45.85/45.09
Q1127-145	GPS[c]	1.18	12	44.91	45.74	46.80	47.06/46.17
Q1143-245	GPS	1.95	26	44.91	44.96	45.75	46.32/45.67
Q1245-197	GPS	1.28	2.1×10^3	44.77	43.89	44.80	45.31/44.91
Q1250+56/3C 277.1	CSS	0.32	3.86×10^3	43.11	43.93	45.23	45.19/44.15
Q1328+254/3C 287	CSS	1.055	200	44.73	44.75	46.10	46.11/45.45
Q1416+067/3C 298	CSS	1.439	6.35×10^3	44.68	45.84	46.90	47.13/46.12
Q1458+718/3C 309.1	CSS	0.905	8.25×10^3	44.63	45.20	47.14	46.52/45.69
Q1815+614	GPS	0.601	...	43.38	43.74	44.70	45.04/44.16
Q1829+290	CSS	0.842	11.86×10^3	44.06	43.23	44.96	44.63/44.16

Notes. Columns: 1: Source name; 2: GPS or CSS radio classification based on O'Dea (1998); 3: redshift; 4: projected jet LS (calculated from O'Dea (1998) with a current cosmology); 5: radio luminosity at 5 GHz (see Siemiginowska et al. 2008, and references therein); 6: X-ray luminosity at 2 keV (Siemiginowska et al. 2008); 7: bolometric luminosity; 8: predicted γ-ray (100 MeV–10 GeV) luminosity (see the text).

[a] Calculated using Equation (5) for a single power-law EED; the scatter is 0.16 (dex).

[b] Calculated using Equation (6) for a broken power-law EED; the scatter is 0.55 (dex).

[c] Classification for this source has been revised (see the text).

observed sample (up to 1–2 orders of magnitude) must be considered to reconcile observations and simulated radio and X-ray luminosities for $L_{\mathrm{jet,kin}}/L_{\mathrm{disk}} = 0.01$. On the other hand, the discrepancy with the simulations becomes even larger if only a fraction of the X-ray emission in the quasars of the sample is produced by the jet.

Interestingly, the simulations show that the lack of a clear correlation between the $L_{5\,\mathrm{GHz}}$ and $L_{2\,\mathrm{keV}}$ luminosities of the observed sample does not necessary rule out a common (jet) origin for them.

In Table 3, we report the 100 MeV–10 GeV luminosities estimated using Equations (5) and (6) (we considered only the $L_{\mathrm{jet,kin}}/L_{\mathrm{disk}} = 1.0$ distribution, which better covers the $L_{5\,\mathrm{GHz}}$ and $L_{2\,\mathrm{keV}}$ of the sample). The predicted γ-ray luminosities span between $\approx 10^{44}$ and $\approx 10^{47}$ erg s^{-1} and the minimum and maximum 100 MeV–10 GeV fluxes are $\sim 4.2 \times 10^{-14}$ erg cm^{-2} s^{-1} and $\sim 2.5 \times 10^{-11}$. In comparison, the three year *Fermi*-LAT flux sensitivity for point sources with 5σ detections is $\sim 3 \times 10^{-12}$ erg cm^{-2} s^{-1} (at the Galactic pole and assuming a power-law spectrum with $\Gamma_\gamma = 2$; see Ackermann et al. 2012). Seven of the estimated γ-ray fluxes using Equation (5) are above or near such a threshold and the number reduces to four for Equation (6). None of the sources in the sample are associated with a γ-ray source in the LAT 2-yr Point Source Catalog (2FGL Nolan et al. 2012, except for PKS 1127-14, associated with the γ-ray source 2FGL1130.3-1448). However, the 2FGL includes only sources with a minimum $\gtrsim 4\sigma$ detection significance.[11]

[11] More specifically, the 2FGL uses Test Statistics, TS, to quantify how significantly the source emerges from the background and imposes a minimum TS of 25, which corresponds to a significance of just over 4σ evaluated from the χ^2 distribution with four degrees of freedom (position and spectral parameters Mattox et al. 1996).

5. *FERMI*-LAT OBSERVATIONS

5.1. Fermi-LAT Data Analysis

The *Fermi*-LAT is a pair-production γ-ray telescope sensitive to photons in the energy range from 20 MeV to >300 GeV. Its large effective area (~8000 cm^{-2} on-axis for $E > 1$ GeV) provides view of 2.4 sr of the full sky with an unprecedented angular resolution at these energies (the 68% containment angles of the reconstructed incoming photon direction below 10 GeV is estimated to be $\theta_{68} \simeq 0.^{\circ}8(\varepsilon_{\gamma}/\mathrm{GeV})^{-0.8}$). It mainly operates in a sky-survey mode and covers the full sky every two orbits (~3 hours). A detailed description of the *Fermi*-LAT and the on-orbit performance are provided in Atwood et al. (2009).

We analyzed the *Fermi*-LAT data collected during 46 months of operation (2008 August to 2012 February). For each source, we selected only the events of the Pass 7 V6 *Source* class, which reduces the residual background rate (see Ackermann et al. 2012). We used the Pass7 version 6 of the instrument response functions (Rando & for the Fermi LAT Collaboration 2009; Ackermann et al. 2012). The data were analyzed with the LAT Science Tools software package (version v9r27p1). We also made use of the LAT Analysis Scripts[12] (version 0.1.9) for part of the analysis.

We applied the standard event selections. Time intervals when the rocking angle of *Fermi*-LAT was greater than 52° were rejected and only events coming from zenith angles smaller than 100° were considered in order to minimize the contribution from terrestrial albedo γ-rays. We considered data in the 0.2–100 GeV energy range. Although conservative, this energy selection allow us to reduce systematic errors and the positional uncertainties.

For each source, we selected a circular region of interest (RoI) of 10° radius, centered on the radio position of our candidate. The full *Fermi* model that we adopted to calculate an unbinned likelihood includes all the point-like and diffuse sources within the RoI. Due to the energy-dependent size of the *Fermi*-LAT point-spread function (PSF), sources falling between 10° and 15° can contribute to the total counts observed in the RoI and therefore were also included in the model. The emission model also accounts for the Galactic and extragalactic (and instrumental) diffuse backgrounds. In this work, we used the "mapcube" file `gal_2yearp7v6_v0.fits` and the `iso_p7v6source.txt` table to describe the emission from the Milky Way and the isotropic component, respectively.

We adopted a power-law spectrum ($F = KE^{-\Gamma_{\gamma}}$) for our sources and assumed the spectral models and parameters reported in the 2FGL for all the other sources. We initially fixed the spectral parameters of all the sources located 5° away from our target to the best-fit value reported in the 2FGL. We performed a fit using the unbinned maximum likelihood (*gtlike*) and evaluated the significance of the source detection based on the TS value[13] (TS; Mattox et al. 1996). When the fit did not converge, we simplified the model in the following way: (1) we fixed the γ-ray photon index of our target to $\Gamma_{\gamma} = 2.5$ and (2) we progressively froze the spectral shape parameters of the sources in the inner 5° circle starting from the farthest ones, and also all the parameters of weak background sources (<10^{-14} phot cm^{-2} s^{-1}).

[12] http://fermi.gsfc.nasa.gov/ssc/data/analysis/scitools/LATAnalysisScripts.html

[13] The TS is the logarithmic ratio of the likelihood of a source being at a given position in a grid to the likelihood of the model without the source: $\mathrm{TS} = 2\log(\mathrm{likelihood}_{\mathrm{src}}/\mathrm{likelihood}_{\mathrm{null}})$.

Table 4
GPS/CSS Sample–*Fermi*-LAT Results

Source	TS[a]	*Fermi*-LAT Flux[b] ($\times10^{-9}$ phot cm^{-2} s^{-1})	*Fermi*-LAT Flux ($\times10^{-12}$ erg cm^{-2} s^{-1})
(1)	(2)	(3)	(4)
Q0134+329	<0	<3.5	<1.51
Q0615+820	3	<4.9	<2.12
Q0740+380	3	<3.7	<1.60
Q0741+311	6	<7.9	<3.41
PKS1127-145	514	63 ± 4[c]	27.30 ± 1.73
Q1143-245	1	<3.1	<1.34
Q1245-197	<0	<2.1	<0.91
Q1250+568	1	<3.6	<1.56
Q1328+254	1	<5.9	<2.55
Q1416+067	3	<8.0	<3.46
Q1458+718	1	<3.6	<1.56
Q1815+6127	<0	<1.2	<0.52
Q1829+290	20	<19.5[d]	<8.42

Notes. Columns: 1: Source name; 2: TS value; 3,4: *Fermi*-LAT 100 MeV–10 GeV fluxes.

[a] When TS < 9 (≈3σ), the reported flux is an upper limit.

[b] Upper limits are calculated in the 100 MeV–10 GeV energy band, for a fixed γ-ray spectral index of 2.5, at a 95% confidence interval.

[c] The measured γ-ray spectral index is 2.75± 0.05.

[d] Contamination of nearby (<3°) γ-ray sources cannot be excluded (see the text and Figure 5), thus even in this case we report the upper limit value.

5.2. Fermi-LAT Results

The results of the *Fermi*-LAT analysis are shown in Table 4. In most of the cases, we did not find γ-ray excesses above the background that coincided with the positions of the sources in the sample. For TS values less than 9 ($\lesssim 3\sigma$), we calculated the corresponding integral flux upper limit in the range 0.1–10 GeV at the 95% confidence level, setting the photon index of the spectral power law equal to $\Gamma_{\gamma} = 2.5$.

When the *Fermi* likelihood analysis returned ambiguous results, we furthermore proceeded with the analysis and investigated (1) the spatial distribution of the TS value (TS map) in the RoI (using *gttsmap*) and (2) the temporal distribution of the TS value by producing a 0.2–100 GeV light curve in the selected period probing a bin time of months. We note that the TS map also allows us to check for the presence of possible new background sources in the 4-yr dataset that are not included in the 2FGL. In the case of Q1829+290, we obtained a TS value of 20. We built a TS map using the best-fit model returned by the likelihood analysis that includes all the sources reported in the 2FGL (without our source). All the parameters of the model were fixed except for the Galactic diffuse prefactor and the isotropic diffuse normalization. The TS map of the residuals (in Figure 5, left panel) shows an excess in the region corresponding to the radio position of Q1829+290 (TS ~ 17). In the source field, there are three 2FGL γ-ray sources within a 3° radius (2FGLJ1829.1+2725 at 1.°76 distance, 2FGLJ1836.2+3137 at 2.°72, and 2FGLJ1842.3+2740 at 2.°83) and, given the *Fermi*-LAT PSF in the selected energy band (≈3° at 200 MeV), we cannot exclude flux contamination. We produced the γ-ray light curve of Q1829+290 using four-month time bins and compared it with the light curves of the two nearest 2FGL sources. In this case, we left only the normalization parameter (the integral and prefactor for the PowerLaw2 and PowerLaw models, respectively) of the three sources (and again the normalizations of the Galactic and isotropic diffuse and instrumental

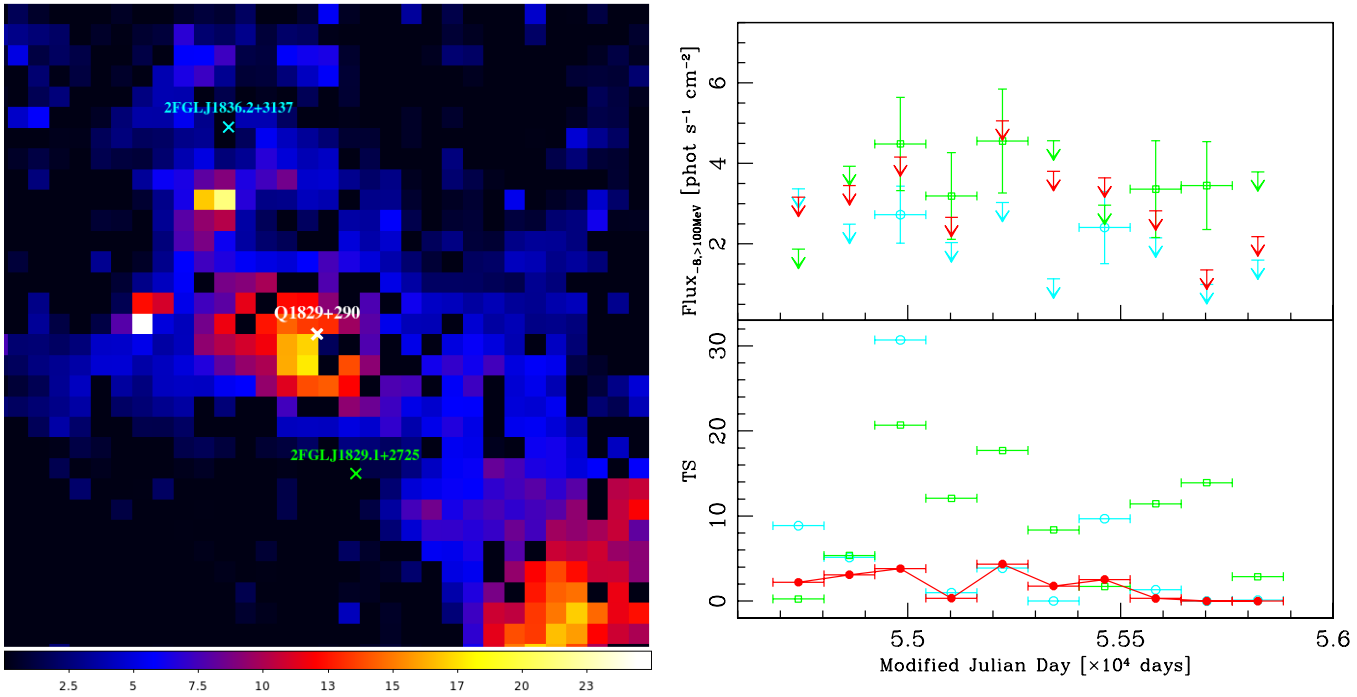

Figure 5. Left panel: *Fermi*-LAT TS map of the residuals obtained from the likelihood best-fit model without Q1829+290, selecting 32×32 pixels with 0.25 degree bins. The position of Q1829+290 and the two nearest 2FGL sources are marked in the map. The position of Q1829+290 coincides with a residual excess (TS ∼ 17). Right panel: *Fermi*-LAT flux light curve of Q1829+290 (in red) and the two nearest γ-ray sources reported in the 2FGL (2FGLJ1829.1+2725 in green and 2FGL1836.2+3137 in cyan) covering the period from 2008 August 4 to 2012 February 23, using a binning time of 4 months (upper panel). Fluxes are reported in units of 10^{-8} phot cm^{-2} s^{-1} and replaced by upper limit values for TS < 9. The lower panel shows the corresponding TS values of the three sources in the time bins. The TS value of Q1829+290 (in red) is below 9 in all the bins.

(A color version of this figure is available in the online journal.)

backgrounds) free to vary. The likelihood analysis was performed in each time interval: the TS values of each of the three sources was computed and for TS < 9 (3σ) the flux value was replaced by the upper limit. The flux light curves of the three sources, together with their TS values in each time bin, are shown in Figure 5. The TS of Q1829+290 is below 9 in all the intervals and its flux fluctuations follow those of the nearest 2FGL source (2FGLJ1829.1+2725), pointing to flux contamination.

PKS1127-14 is the only object associated with a γ-ray source with a high TS value (514). However, the classification of this source has been revised from a GPS to a FSRQ (Healey et al. 2007). Its γ-ray light curve shows variability, further supporting the interpretation of a blazar-like nature of the core. We refer to our future paper for a detailed analysis of this source (see also Abdo et al. 2010a).

Summarizing, there was no statistically significant γ-ray detection of the young radio sources in our sample for the considered *Fermi*-LAT dataset. In the case of Q1829+290, i.e., the only source with a TS value above 9, we cannot exclude flux contamination from near sources in the field.

6. DISCUSSION

The primary goal of the study is to investigate the nature of the high-energy emission produced by the jet in young radio sources focusing for the first time on the γ-ray band. The SED simulations have shown that jets of compact sources can be γ-ray luminous: intrinsically powerful jets observed at moderate angles ($\theta \geqslant 10^\circ$) could reach $L_{100\,\mathrm{MeV}-10\,\mathrm{GeV}} \sim 10^{48}$ erg s^{-1}. The identification of γ-ray luminous young sources is, however, not straightforward, due to our limited knowledge of some of the jet parameters (e.g., Γ, θ). Radio and X-ray observations are both necessary to select γ-ray candidates among young and bright radio sources ($L_{5\,\mathrm{GHz}} \gtrsim 10^{42}$ erg s^{-1}). In the following, we compare the model predictions and observations for the selected sample of young radio quasars and discuss the implications for the jet emission.

6.1. Model Predictions and LAT Upper Limits

The analysis of the *Fermi*-LAT observations did not reveal γ-ray emission associated with the sources in our sample. However, a jet contribution to the high-energy emission is not ruled out. In Figure 6, the *Fermi*-LAT upper limits are compared with the simulated γ-ray luminosities, $L_{100\,\mathrm{MeV}-10\,\mathrm{GeV}}$, as a function of the LS (for the observed sample, we used the projected jet LS[14] derived from the radio data and reported in Table 3). For this comparison, we selected subsamples from each simulated distribution so that the radio and X-ray luminosities are in the range of the observed sample: $10^{43} \leqslant L_{5\,\mathrm{GHz}} \leqslant 10^{45}$ erg s^{-1}, $10^{43} \leqslant L_{2\,\mathrm{keV}} \leqslant 10^{46}$ erg s^{-1} (and $10^{45} \leqslant L_{\mathrm{bol/disk}} \leqslant 10^{47}$ erg s^{-1}, 10 pc $\leqslant$ LS $\leqslant$ 10 kpc).

The luminosity selection determines a progressive reduction of the number of simulated sources with increasing LS. Specifically, in the subsamples obtained from $L_{\mathrm{jet,kin}}/L_{\mathrm{disk}} = 0.1$ and 0.01, there are no sources with LSs larger than ∼5 kpc and ∼200 pc, respectively. The reason is that the radiative efficiency of the jet depends on LS ($L'_{\mathrm{syn}} \propto \mathrm{LS}^{-1}$, $L'_{\mathrm{EC}} \propto \mathrm{LS}^{-1}$, and $L'_{\mathrm{SSC}} \propto \mathrm{LS}^{-2}$), thus for the considered parameter intervals only the most powerful jets ($L_{\mathrm{jet,kin}} \gtrsim 10^{46}$ erg s^{-1}) can produce the observed radio and X-ray luminosities at kiloparsec scales.

[14] For the rest of the discussion, we excluded from the sample Q1815+6127 which, to our knowledge, has no LS measure reported in the literature.

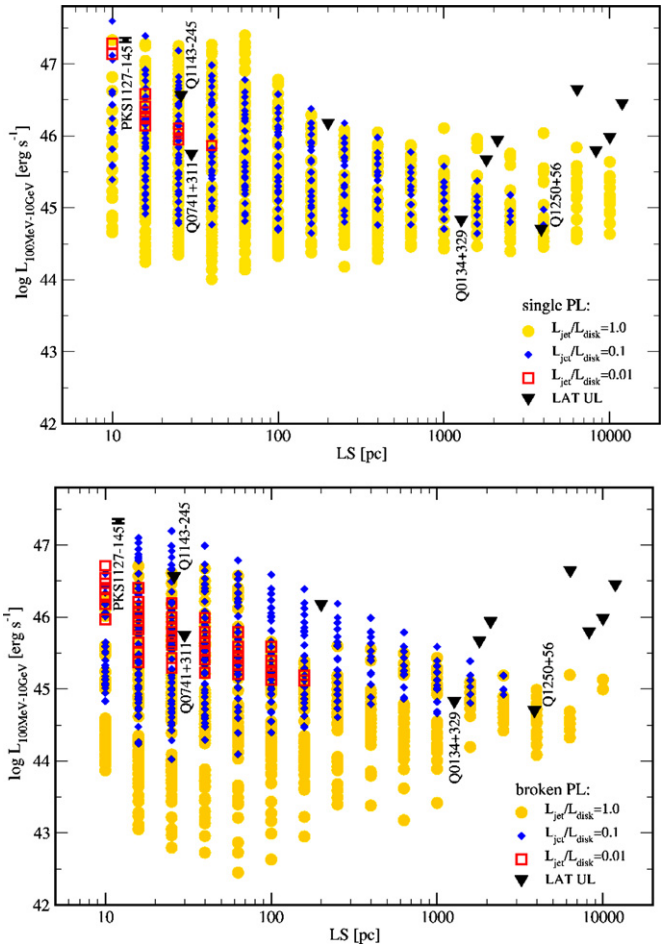

Figure 6. Simulated 100 MeV–10 GeV luminosities and *Fermi*-LAT results are plotted as a function of LS. Black solid triangles indicate flux upper limits (calculated between 100 MeV and 10 GeV for a 95% confidence limit), yellow solid circles are the simulated sources assuming $L_{\rm jet,kin} = L_{\rm disk}$, the blue solid diamonds are the simulated sources for $L_{\rm jet,kin} = 0.1 L_{\rm disk}$, and the red empty squares are for $L_{\rm jet,kin} = 0.01 L_{\rm disk}$. PKS1127-145 is the only source detected by *Fermi*-LAT. Here, a subsample of each simulated distribution is selected in the range of the observed radio ($10^{43} \lesssim L_{5\,\rm GHz} \lesssim 10^{45}$ erg s^{-1}) and X-ray ($10^{43} \lesssim L_{2\,\rm keV} \lesssim 10^{46}$ erg s^{-1}) luminosities of the GPS/CSS quasar sample (see the text). The upper panel shows the simulated luminosities assuming a single power-law EED and the lower panel assumes a broken power-law EED.

(A color version of this figure is available in the online journal.)

The simulated γ-ray luminosities in the subsamples are compatible with the *Fermi*-LAT upper limits, although the *Fermi*-LAT sensitivity is the main limit for a test of the model predictions. For a few sources, the comparison between observations and simulations (in the case of a single power-law EED) allows one to place constraints on the jet parameters (upper panel in Figure 6). The *Fermi*-LAT limits on Q1143-245 and Q0741+311 rule out the most extreme simulated γ-ray luminosities ($L_{100\,\rm MeV-10\,GeV} \gtrsim 10^{46}$–$10^{47}$ erg s^{-1}). A jet with $L_{\rm jet,kin}/L_{\rm disk} = 0.01$ also appears to produce $L_{100\,\rm MeV-10\,GeV}$ above the *Fermi*-LAT upper limit of Q0741+311. Similarly, a *Fermi*-LAT detection of Q0134+329 and Q1250+56 would be likely if the jet has $L_{\rm jet,kin}/L_{\rm disk} = 1.0$ (in the single power-law EED case).

The γ-ray luminosity associated with PKS 1127-14, $L_{100\,\rm MeV-10\,GeV} = 2.16 \times 10^{47}$ erg s^{-1}, is consistent with the highest predicted γ-ray luminosities for the single power-law EED (upper panel in Figure 6). The LS adopted for this source (LS = 12 pc, from O'Dea 1998) refers to its initial GPS classification (and corresponds to the inner part of the radio jet). Such a value can be considered as an upper limit for the distance of the emitting region from the BH. In fact, the location of the γ-ray-emitting region in blazar sources is under debate and estimates span from sub-parsec to a few tens of parsecs (see Sikora et al. 2009 for a discussion and the cases of the quasar PKS 1510-089 and the BL Lacertae object OJ287 in Marscher et al. 2010 and Agudo et al. 2011, respectively). Interestingly, Błażejowski et al. (2004) proposed that the γ-ray emission of PKS 1127-14 is produced via Compton scattering on the IR photons taking place on pc scales (Błażejowski et al. 2004). In our simulated distributions, γ-ray luminosities of the order of 10^{46}–10^{47} erg s^{-1} are obtained via EC/dust in compact (LS $\lesssim$ 20 pc) and powerful jets ($L_{\rm jet,kin} \gtrsim 10^{46}$ erg s^{-1}). For these parameter values, the emitting region is still moving through the medium that produces the IR photons ($L_{\rm dust} \gtrsim 10^{46}$ erg s^{-1}). The highest EC/dust luminosities (in the observers rest frame) are produced for jet bulk motions of $\sim$2–4. For the considered minimum viewing angle ($\theta = 10^{\circ}$), large values of Γ (e.g., 10–20) would narrow the radiation cone and reduce the observed luminosity. The observed γ-ray luminosity of PKS 1127-14 can be reproduced by assuming a single power law for the EED (for all the $L_{\rm jet,kin}/L_{\rm disk}$ ratios), while it is underpredicted in the broken power-law scenario (although within an order of magnitude). Nonetheless, we note that the high-energy SED of blazars inferred from X-ray to γ-ray observations typically displays a complex shape (Abdo et al. 2010a; Giommi et al. 2012) and a broken power law appears to be a more realistic description of the energy distribution of the radiating particles.

6.2. X-Rays: Model Predictions and Observations

We consider the same subsamples of simulated sources to test the model predictions against observations in the X-ray band. In Figure 7, we show the simulated and observed $L_{2\,\rm keV}$ to $L_{5\,\rm GHz}$ ratios as a function of LS. The simulated ratios have a different evolution with LS depending on the shape of the EED. In the broken power-law case, the maximum $L_{2\,\rm keV}$ to $L_{5\,\rm GHz}$ ratio decreases with LS. Two connected effects cause this trend: (1) at large LS ($\gtrsim$1 kpc), intrinsically powerful jets ($L_{\rm jet,kin} \gtrsim 10^{46}$–$10^{47}$ erg s^{-1} and thus $L_{\rm jet,kin}/L_{\rm disk} \geqslant 0.1$) are needed to produce the observed radio and X-ray luminosities of the CSS quasars and (2) the X-ray emission of such powerful jets is dominated by the SSC component, thus $L_{2\,\rm keV}/L_{5\,\rm GHz}$ scales as $L'_{\rm SSC}/L'_{\rm syn} \propto {\rm LS}^{-1}$ at all the considered LSs.

For the single power-law EED, the maximum $L_{2\,\rm keV}/L_{5\,\rm GHz}$ is (roughly) constant for LS $\gtrsim$ 100 pc (for $L_{\rm jet,kin}/L_{\rm disk} = 1.0$; see the upper panel in Figure 7). Above such LSs, the EC/disk and EC/dust contributions to the X-ray band become dominant over the SSC (see also Figure 1) and thus $L_{2\,\rm keV}/L_{5\,\rm GHz} \propto L'_{\rm EC}/L'_{\rm syn} \propto {\rm LS}^{0}$. When $L_{\rm jet,kin}/L_{\rm disk} < 1.0$, the relative intensity of the disk-related photon fields ($U'_{\rm disk}$ and $U'_{\rm dust}$) with respect to the local synchrotron emission ($U'_{\rm syn}$) increases, therefore the transition to a constant $L_{2\,\rm keV}$–$L_{5\,\rm GHz}$ ratio (i.e., $L_{\rm EC} \gtrsim L_{\rm SSC}$ in X-rays) happens at smaller LSs than for $L_{\rm jet,kin}/L_{\rm disk} = 1.0$.

The modeled $L_{2\,\rm keV}$–$L_{5\,\rm GHz}$ ratios for LS $\lesssim$ 1 kpc are in good agreement with the ones of the quasar sample. At kiloparsec scales, the model underestimates the $L_{2\,\rm keV}$–$L_{5\,\rm GHz}$ ratios observed in CSS quasars (see Figure 7). The discrepancy is caused by the fact that the simulated sources with LS $\gtrsim$ 1 kpc have X-ray luminosities only marginally comparable with, or below, the observed ones but can be radio luminous, with $L_{5\,\rm GHz}$ of the order of $\sim 10^{44}$ erg s^{-1} or larger. This result is not in

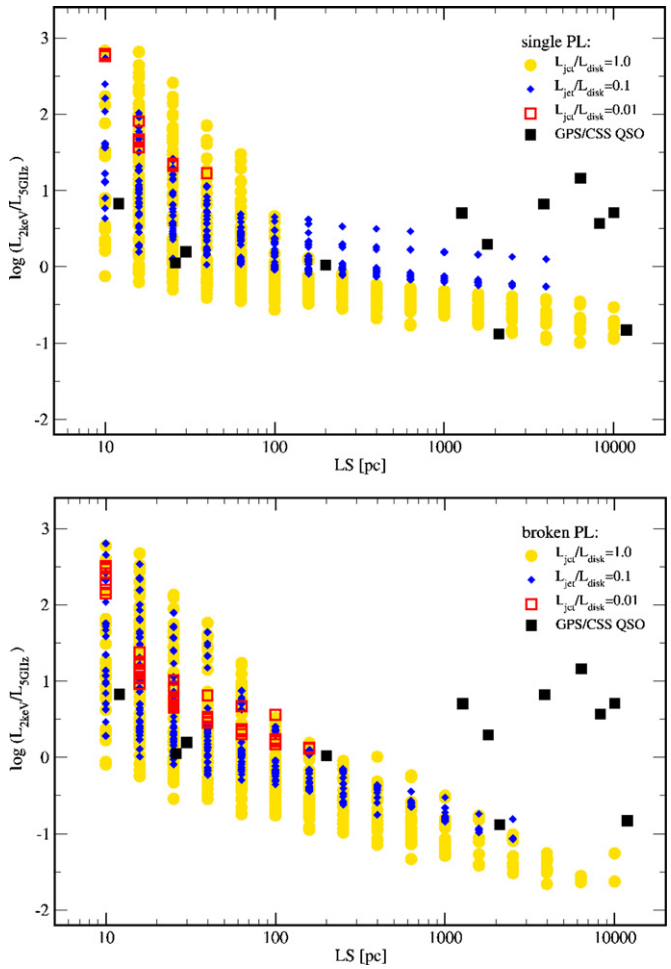

Figure 7. Comparison of the 2 keV to 5 GHz luminosity ratio as a function of LS for the simulated distributions and the sample of GPS/CSS quasars. Yellow solid circles are for simulations with $L_{\rm jet,kin} = L_{\rm disk}$, blue solid diamonds are for $L_{\rm jet,kin}/L_{\rm disk} = 0.1$, and red empty squares are for $L_{\rm jet,kin}/L_{\rm disk} = 0.01$. Black solid squares are the GPS/CSS quasars in the sample observed by *Chandra* (Siemiginowska et al. 2008). Here, a subsample of each simulated distribution is selected in the range of the observed radio ($10^{43} \lesssim L_{5\,\rm GHz} \lesssim 10^{45}$ erg s^{-1}) and X-ray ($10^{43} \lesssim L_{2\,\rm keV} \lesssim 10^{46}$ erg s^{-1}) luminosities of the GPS/CSS quasar sample (see the text). In the upper (lower) panel, sources are simulated assuming a single (broken) power shape for the EED.

(A color version of this figure is available in the online journal.)

contradiction with the substantial overlap between simulated and observed sources shown in Figure 4. In fact, in that case, the comparison is limited to two observables only ($L_{5\,\rm GHz}$ and $L_{2\,\rm keV}$), while in Figure 7 we introduce additional information (i.e., the LS and the relation between the radio and X-ray jet luminosities, i.e., $L_{2\,\rm keV}/L_{5\,\rm GHz}$).

The gap between the observed and simulated sources, although still present, is reduced for the subsamples simulated assuming a single power-law EED and when $L_{\rm jet}/L_{\rm disk} = 0.1$. However, in the $L_{\rm jet,kin}/L_{\rm disk} = 0.1$ distribution, the number of kiloparsec-scale sources, which abide by the subsample selection criteria, is limited. We also note that the difference between simulated and observed $L_{2\,\rm keV}$–$L_{5\,\rm GHz}$ ratios could be even more severe when we consider the true, i.e., not the projected, LS.

6.2.1. Parameter Values and Assumptions

Bearing in mind the limited size of our sample, we can discuss the differences between the model and observations. We first consider whether different parameter values and assumptions might change the predictions.

A more compact emitting region than the one assumed here ($R = 0.1$ LS) would increase the SSC luminosity. We tested the case of $R = 0.01 \times$ LS. The $L_{2\,\rm keV}$ –$L_{5\,\rm GHz}$ ratios increase but at kiloparsec scales they are still below the observed ratios.

Can different Doppler factors, δ, modify the model results in the right directions? In our simulations, δ is between ∼0.3 and ∼5. For the considered values of θ (10°–50°), which reasonably sample the viewing angles for quasars, Γ above the maximum assigned value of 10 would not increase δ. Furthermore, the observed SSC and synchrotron flux densities have the same dependency on δ. Thus, this factor cannot significantly modify the $L_{5\,\rm GHz}/L_{2\,\rm keV}$ of jets where the SSC luminosity dominates the X-ray emission. The boosting of the external Compton luminosity depends on the arrival direction of the seed photons in the jet comoving frame (Dermer 1995). If the emitting region is still within the putative torus region, for instance, there is a $\sim\delta^{1+\alpha}$ factor between the EC/dust and the synchrotron observed luminosities. However, for the considered external fields, such an effect could be important for small sources (tens of parsecs), without affecting the ratios in the CSS sample.

The discrepancy between observations and simulations holds true for all the simulated subsamples, although to different degrees, suggesting that it does not strongly depend on the assumed spectral shape of the electron distribution.

An increase of the particle-to-magnetic field energy density ratio is a viable option. In Figure 8, we show that simulations assuming $U'_e/U'_B \gtrsim 10^3$ (and $L_{\rm jet,kin} = L_{\rm disk}$) can reproduce the observed $L_{2\,\rm keV}$–$L_{5\,\rm GHz}$ ratios. Interestingly, the corresponding simulated γ-ray luminosities for the majority of the sources are above the measured *Fermi*-LAT upper limits and would make a γ-ray detection likely.

6.3. Origin of the X-Ray Emission

The study of the parameters seems to confirm that the observed X-ray emission can be hardly produced by the jet at scales larger than ∼1 kpc. This can be interpreted in two ways: (1) the bulk of the jet X-ray emission is always produced at distances smaller than ∼1 kpc from the central BH and (2) the observed X-ray emission is due to an additional component not related to the jet, such as the disk-corona emission.

In our model, the dissipation region moves along the jet as the source expands: the decrease of the X-ray emission with LS is a consequence of the increasing volume of the emitting region and a decrease of the intensities of the nuclear photon field ($\propto 1/\rm LS^2$). This is certainly a simplified picture, since large (>10 kpc) radio jets may display multiple X-ray knots and diffuse X-ray emission. However, in our simulations, the case of a bright knot located at an intermediate position along an extended jet is accounted for by considering a distribution of LSs[15] (e.g., a knot located at 100 pc in a 10 kpc jet will have the same luminosity as a 100 pc jet with the same jet power). Continuous X-ray emission is typically present at lower luminosity levels and here we aim at modeling the brightest X-ray component of a jet.

Stanghellini et al. (2005) found that in GPS quasars, the origin of the radio emission appears to be close to the core. This means that either the bulk of the emission is produced by the inner part of the jet or, as pointed out by the authors, it is due to projection

[15] We do not assume any condition specific to the jet termination for the knot emission.

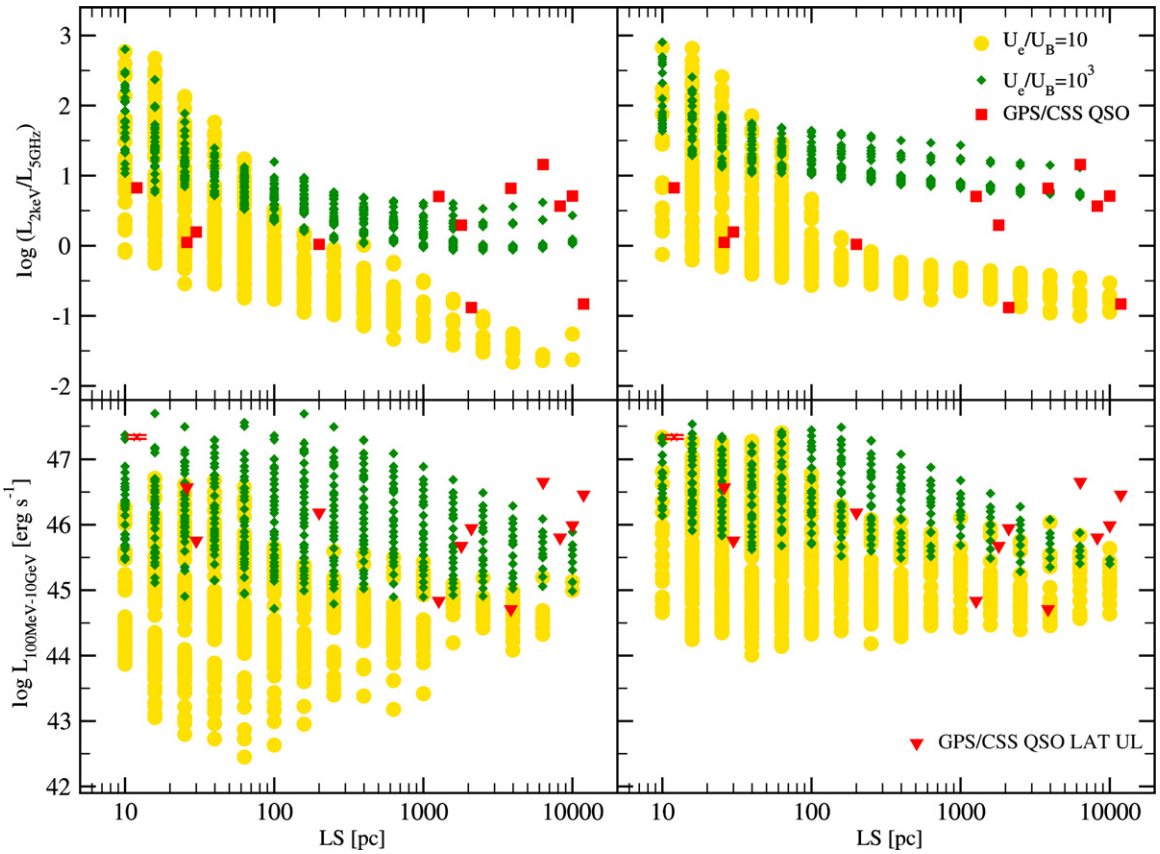

Figure 8. Upper panels: $L_{2\,\mathrm{keV}} - L_{5\,\mathrm{GHz}}$ ratios are shown as a function of LS for simulated sources and the sample of GPS/CSS quasars (red solid squares). Lower panels: simulated 100 MeV–10 GeV luminosities and *Fermi*-LAT upper limits (red solid triangles) plotted as a function of LS. The left panels show simulations assuming a broken power-law EED and right panels show a single power-law EED. The yellow solid circles are the simulated sources when $U_e/U_B = 10$ while the green solid diamonds for $U_e/U_B = 10^3$. In all simulations, $L_{\mathrm{jet,kin}} = L_{\mathrm{disk}}$ is assumed. Subsamples have been selected from the distributions, as described in the text. (A color version of this figure is available in the online journal.)

effects making the compact and young nature of these sources uncertain. Salvesen et al. (2009) investigated the origin of the X-ray emission observed in the GPS quasar 3C 287 and concluded that it is likely associated with the inner radio jet, whose axis is closely aligned to the observers line of sight. The authors argue that the lack of variability, which is typical of blazar sources, might be related to particular physical conditions of the jet in the initial phase. In this scenario, the non-detection with *Fermi*-LAT can also be in favor of a non-blazar nature. In the CSS quasar 3C 48, Worrall et al. (2004) reported the presence of a hard X-ray excess that is ascribed to the inner part of the jet and a similar explanation is invoked for the CSS source PKS 2004-447 (Gallo et al. 2006).

As an alternative, the X-ray emission may be primarily contributed by thermal radiation from the innermost region of the accretion disk or Comptonization of the disk photons in a hot corona, as observed in the X-ray cores of quasars and FRII radio galaxies. Siemiginowska et al. (2008) found that the median optical-to-X-ray luminosity parameter (α_{oX}) for their sample of GPS and CSS quasars and radio galaxies is 1.53 ± 0.24, in agreement with α_{oX} of radio-quiet quasars (Kelly et al. 2007). In addition, the estimated disk luminosities of the observed quasars suggest a radiatively efficient disk. An accretion-related origin is also plausible for the X-ray emission of GPS radio galaxies, which appears to be highly absorbed (with an equivalent hydrogen column density of $N_{\mathrm{H}} > 10^{22}$ cm^{-2}, Guainazzi et al. 2006; Vink et al. 2006; Siemiginowska et al. 2008; Tengstrand et al. 2009). An alternative explanation in the framework of non-thermal emission from the lobes is proposed by Stawarz et al. (2008) and Ostorero et al. (2010).

6.4. Comparison with γ-ray-detected Misaligned AGNs

A comparison with non-blazar radio sources detected in γ-rays is useful to understand how the jet emission can contribute the X-ray to γ-ray band. Here, we consider the recent γ-ray studies on misaligned active galactic nuclei (MAGNs) and Broad Line Radio Galaxies (BLRGs; Abdo et al. 2010b; Kataoka et al. 2011; Grandi et al. 2012). The sample of MAGNs observed by *Fermi*-LAT is dominated by low-power FRI radio sources, while powerful FRII appear to be an elusive γ-ray class. The different redshift distribution of the two classes, with FRII being (typically) more distant, seems not sufficient to explain the low rate of detection. An intrinsic difference in the jet structure and/or emission mechanism responsible for the γ-rays has been proposed as a possible explanation (Grandi et al. 2012, and references therein). Jets with a complex dynamical structure as well as beaming differences between SSC and EC (Georganopoulos & Kazanas 2003; Ghisellini et al. 2005; Giannios et al. 2010) processes can account for a smaller number of FRII sources than FRI sources. Among the 18 BLRGs investigated in Kataoka et al. (2011) using two-year *Fermi*-LAT data, only 3C 111 and 3C 120 have γ-ray detections. In these sources, the γ-ray emission is ascribed to the unresolved cores and displays variability on month (or longer) timescales, with the consequence that the sources are not always γ-ray-detected.

The sources in our sample are all radio powerful and most of them morphologically resemble FRII radio sources. Thus, it is possible that they share the same γ-ray elusiveness. The results of our study are in agreement with previous findings that the jet does not likely dominate the X-ray core emission. In BLRG cores, the jet emission can contribute to some fraction of the X-ray emission but it is typically hidden by the emission of the accretion disk and corona (Zdziarski & Grandi 2001; Grandi & Palumbo 2007; Kataoka et al. 2007; Sambruna et al. 2009). In the 2–10 keV band, Grandi & Palumbo (2007) constrain the jet to accretion flow relative contribution to a factor of <0.7. Nonetheless, the jet might emerge at higher energies, as confirmed by the γ-ray detections of 3C 111 and 3C 120. Kataoka et al. (2011) evaluate the jet and disk relative contributions in the selected BLRGs using a composite model of a thermal plus non-thermal templates to reproduce the broadband core emission (similar to the approach adopted in Grandi & Palumbo 2007). The authors conclude that the total (observed) luminosity of the jet is on average not less than 1% of the disk-corona luminosity and in some sources can even be almost comparable to it.

7. SUMMARY

We investigated the high-energy emission produced by jets in young radio quasars, focusing on a sample of GPS and CSS quasars previously detected in X-rays by *Chandra*. The analysis of ∼46 month *Fermi*-LAT data does not reveal any statistically significant γ-ray detection of the sources, except for the already known case of PKS1127-14. For the first time, we compared the *Fermi*-LAT and *Chandra* observations of the sample to γ-ray and X-ray luminosities predicted by a simple jet synchrotron and IC radiative model. The simulations performed for a reasonable set of model parameters and assumptions have shown the following for the analyzed sample.

1. $L_{\rm jet,kin}/L_{\rm disk} > 0.01$ is required for the range of disk luminosities of the sources: low-power jets (as for the $L_{\rm jet,kin}/L_{\rm disk} = 0.01$ case) fail to produce the majority of the observed radio luminosities (Figure 4);
2. A jet origin of the bulk of the observed X-ray emission is strongly disfavored. Specifically, this holds true for X-ray emission associated with kpc jets (i.e., jets of CSS quasars) even when we significantly change our initial assumptions;
3. Large deviations from energy equipartition ($U'_e/U'_B \gg 10$), necessary to produce the observed X-ray luminosities, would imply γ-ray fluxes detectable by *Fermi*-LAT.

Our analysis indicates that in the considered sample, the bulk of the X-ray emission is either related to the inner (<1 kpc) jet or to a different component, most likely the disk-corona.

This study also shows that the γ-ray band can be important for the classification of compact radio sources, to distinguish between young and aligned sources: a GPS quasar that is radio and X-ray bright but not detected in γ-rays (at the current level of the LAT all-sky survey sensitivity) is likely to be truly a young compact radio source rather than a blazar with large radio structures observed at small viewing angles.

The authors thank M. Sikora and D. E. Harris for useful suggestions and comments. We are grateful to the anonymous referee for critical comments that helped to improve the paper. This work was supported by the National Aeronautics and Space Administration contract NAS8-03060 and under the following grants: NNX10AO60G issued through the Fermi Guest Observer Program and GO1-12145X issued through the Chandra X-Ray Observatory Guest Observer program. Ł.S. was supported by Polish NSC grant DEC-2012/04/A/ST9/00083. The authors thank the Fermi Science Support Center Help Desk team for support in the data analysis. This research has made used of TOPCAT[16] (Taylor 2005) for the preparation and manipulation of the tabular data.

REFERENCES

Abdo, A. A., Ackermann, M., Ajello, M., et al. 2010a, ApJ, 716, 835
Abdo, A. A., Ackermann, M., Ajello, M., et al. 2010b, ApJ, 720, 912
Ackermann, M., Ajello, M., Albert, A., et al. 2012, ApJS, 203, 4
Agudo, I., Jorstad, S. G., Marscher, A. P., et al. 2011, ApJL, 726, L13
Alexander, P. 2000, MNRAS, 319, 8
Atwood, W. B., Abdo, A. A., Ackermann, M., et al. 2009, ApJ, 697, 1071
Bechtold, J., Elvis, M., Fiore, F., et al. 1994, AJ, 108, 759
Begelman, M. C. 1996, in Cygnus A—Study of a Radio Galaxy, ed. C. L. Carilli & D. E. Harris (Cambridge: Cambridge Univ. Press), 209
Begelman, M. C. 1999, The Most Distant Radio Galaxies, ed. H. J. A. Röttgering, P. N. Best, & M. D. Lehnert, 173
Belsole, E., Worrall, D. M., & Hardcastle, M. J. 2006, MNRAS, 366, 339
Bicknell, G. V., Dopita, M. A., & O'Dea, C. P. O. 1997, ApJ, 485, 112
Bicknell, G. V., & Sutherland, R. S. 2006, AN, 327, 235
Błażejowski, M., Siemiginowska, A., Sikora, M., Moderski, R., & Bechtold, J. 2004, ApJL, 600, L27
Błażejowski, M., Sikora, M., Moderski, R., & Madejski, G. M. 2000, ApJ, 545, 107
Celotti, A., & Ghisellini, G. 2008, MNRAS, 385, 283
Celotti, A., Ghisellini, G., & Chiaberge, M. 2001, MNRAS, 321, L1
Cleary, K., Lawrence, C. R., Marshall, J. A., Hao, L., & Meier, D. 2007, ApJ, 660, 117
Dallacasa, D., Stanghellini, C., Centonza, M., & Fanti, R. 2000, A&A, 363, 887
Dermer, C. D. 1995, ApJL, 446, L63
Dermer, C. D., Schlickeiser, R., & Mastichiadis, A. 1992, A&A, 256, L27
Fanaroff, B. L., & Riley, J. M. 1974, MNRAS, 167, 31P
Fanti, C., Fanti, R., Dallacasa, D., et al. 1995, A&A, 302, 317
Fanti, R., Fanti, C., Schilizzi, R. T., et al. 1990, A&A, 231, 333
Gallo, L. C., Edwards, P. G., Ferrero, E., et al. 2006, MNRAS, 370, 245
Georganopoulos, M., & Kazanas, D. 2003, ApJL, 589, L5
Ghisellini, G., & Tavecchio, F. 2009, MNRAS, 397, 985
Ghisellini, G., Tavecchio, F., & Chiaberge, M. 2005, A&A, 432, 401
Ghisellini, G., Tavecchio, F., Foschini, L., et al. 2010, MNRAS, 402, 497
Giannios, D., Uzdensky, D. A., & Begelman, M. C. 2010, MNRAS, 402, 1649
Giommi, P., Polenta, G., Lähteenmäki, A., et al. 2012, A&A, 541, A160
Godfrey, L. E. H., Bicknell, G. V., Lovell, J. E. J., et al. 2009, ApJ, 695, 707
Grandi, P., & Palumbo, G. G. C. 2007, ApJ, 659, 235
Grandi, P., Torresi, E., & on behalf of the FERMI-LAT collaboration, 2012, arXiv:1205.1686
Grandi, P., Torresi, E., & Stanghellini, C. 2012, ApJL, 751, L3
Guainazzi, M., Siemiginowska, A., Stanghellini, C., et al. 2006, A&A, 446, 87
Hatziminaoglou, E., Fritz, J., Franceschini, A., et al. 2008, MNRAS, 386, 1252
Healey, S. E., Romani, R. W., Taylor, G. B., et al. 2007, ApJS, 171, 61
Holt, J., Tadhunter, C. N., & Morganti, R. 2008, MNRAS, 387, 639
Holt, J., Tadhunter, C. N., Morganti, R., & Emonts, B. H. C. 2011, MNRAS, 410, 1527
Ito, H., Kino, M., Kawakatu, N., & Yamada, S. 2011, ApJ, 730, 120
Kataoka, J., Reeves, J. N., Iwasawa, K., et al. 2007, PASJ, 59, 279
Kataoka, J., & Stawarz, Ł. 2005, ApJ, 622, 797
Kataoka, J., Stawarz, Ł., Takahashi, Y., et al. 2011, ApJ, 740, 29
Kelly, B. C., Bechtold, J., Siemiginowska, A., Aldcroft, T., & Sobolewska, M. 2007, ApJ, 657, 116
Kino, M., & Asano, K. 2011, MNRAS, 412, L20
Kino, M., Ito, H., Kawakatu, N., & Nagai, H. 2009, MNRAS, 395, L43
Kino, M., Ito, H., Kawakatu, N., & Orienti, M. 2013, ApJ, 764, 134
Kunert-Bajraszewska, M., Gawroński, M. P., Labiano, A., & Siemiginowska, A. 2010, MNRAS, 408, 2261
Kunert-Bajraszewska, M., Labiano, A., Siemiginowska, A., & Guainazzi, M. 2013, arXiv:1311.6633
Labiano, A. 2008, A&A, 488, L59
Liuzzo, E., Buttiglione, S., Giovannini, G., et al. 2013, A&A, 550, A76

[16] http://www.star.bris.ac.uk/∼mbt/topcat/

Marscher, A. P., Jorstad, S. G., Larionov, V. M., et al. 2010, ApJL, 710, L126
Mattox, J. R., Bertsch, D. L., Chiang, J., et al. 1996, ApJ, 461, 396
Migliori, G., Siemiginowska, A., & Celotti, A. 2012, ApJ, 749, 107
Mullin, L. M., & Hardcastle, M. J. 2009, MNRAS, 398, 1989
Nolan, P. L., Abdo, A. A., Ackermann, M., et al. 2012, ApJS, 199, 31
O'Dea, C. P. 1998, PASP, 110, 493
Orienti, M. 2009, AN, 330, 167
Orienti, M., & Dallacasa, D. 2008, A&A, 487, 885
Orienti, M., Murgia, M., & Dallacasa, D. 2010, MNRAS, 402, 1892
Ostorero, L., Moderski, R., Stawarz, Ł., et al. 2010, ApJ, 715, 1071
Perlman, E. S., Georganopoulos, M., May, E. M., & Kazanas, D. 2010, ApJ, 708, 1
Rando, R., & for the Fermi LAT Collaboration, 2009, arXiv:0907.0626
Rawlings, S., & Saunders, R. 1991, Natur, 349, 138
Reynolds, C. S., & Begelman, M. C. 1997, ApJL, 487, L135
Salvesen, G., Miller, J. M., Cackett, E., & Siemiginowska, A. 2009, ApJ, 692, 753
Sambruna, R. M., Reeves, J. N., Braito, V., et al. 2009, ApJ, 700, 1473
Siemiginowska, A. 2009, AN, 330, 264
Siemiginowska, A., Bechtold, J., Aldcroft, T. L., et al. 2002, ApJ, 570, 543
Siemiginowska, A., Cheung, C. C., LaMassa, S., et al. 2008, ApJ, 684, 811
Siemiginowska, A., Stawarz, Ł., Cheung, C. C., et al. 2007, ApJ, 657, 145
Siemiginowska, A., Stawarz, Ł., Cheung, C. C., et al. 2012, ApJ, 750, 124
Sikora, M., Begelman, M. C., & Rees, M. J. 1994, ApJ, 421, 153
Sikora, M., Błażejowski, M., Moderski, R., & Madejski, G. M. 2002, ApJ, 577, 78
Sikora, M., Stawarz, Ł., Moderski, R., Nalewajko, K., & Madejski, G. M. 2009, ApJ, 704, 38
Sironi, L., & Spitkovsky, A. 2011, ApJ, 726, 75
Snellen, I. A. G., Schilizzi, R. T., Miley, G. K., et al. 2000, MNRAS, 319, 445
Stanghellini, C., Dallacasa, D., O'Dea, C. P., et al. 2001, A&A, 377, 377
Stanghellini, C., O'Dea, C. P., Dallacasa, D., et al. 2005, A&A, 443, 891
Stawarz, Ł., Cheung, C. C., Harris, D. E., & Ostrowski, M. 2007, ApJ, 662, 213
Stawarz, Ł., Ostorero, L., Begelman, M. C., et al. 2008, ApJ, 680, 911
Stawarz, Ł., Sikora, M., & Ostrowski, M. 2003, ApJ, 597, 186
Tadhunter, C. 2007, NewAR, 51, 153
Tanaka, Y. T., Stawarz, Ł., Thompson, D. J., et al. 2011, ApJ, 733, 19
Taylor, M. B. 2005, in ASP Conf. Ser. 347, Astronomical Data Analysis Software and Systems XIV, ed. P. Shopbell, M. Britton, & R. Ebert (San Francisco, CA: ASP), 29
Tengstrand, O., Guainazzi, M., Siemiginowska, A., et al. 2009, A&A, 501, 89
Tinti, S., Dallacasa, D., de Zotti, G., Celotti, A., & Stanghellini, C. 2005, A&A, 432, 31
Vink, J., Snellen, I., Mack, K.-H., & Schilizzi, R. 2006, MNRAS, 367, 928
Wagner, A. Y., Bicknell, G. V., & Umemura, M. 2012, ApJ, 757, 136
Worrall, D. M., Hardcastle, M. J., Pearson, T. J., & Readhead, A. C. S. 2004, MNRAS, 347, 632
Zdziarski, A. A., & Grandi, P. 2001, ApJ, 551, 186